RSC Advances

REVIEW

View Article Online
View Journal | View Issue

Cite this: *RSC Adv.*, 2022, **12**, 27746

A review on the characterization of metal active sites over Cu-based and Fe-based zeolites for NH_3-SCR

Jialing Chen, *[a] Wei Huang,[a] Sizhuo Bao,[a] Wenbo Zhang,[a] Tingyu Liang,*[b] Shenke Zheng,[c] Lan Yi,[a] Li Guo [a] and Xiaoqin Wu*[a]

Cu-based and Fe-based zeolites are promising catalysts for NH_3-SCR due to their high catalytic activity, wide temperature window and good hydrothermal stability, while the detailed investigation of NH_3-SCR mechanism should be based on the accurate determination of active metal sites. This review systematically summarizes the qualitative and quantitative determination of metal active sites in Cu-based or Fe-based zeolites for NH_3-SCR reactions based on advanced characterization methods such as UV-vis absorption (UV-vis), temperature-programmed reduction with H_2 (H_2-TPR), X-ray photoelectron spectroscopy (XPS), X-ray absorption fine structure spectroscopy (XAFS), Infrared spectroscopy (IR), Electron paramagnetic resonance (EPR), Mössbauer spectroscopy and DFT calculations. The application and limitations of different characterization methods are also discussed to provide insights for further study of the NH_3-SCR reaction mechanism over metal-based zeolites.

Received 15th August 2022
Accepted 20th September 2022

DOI: 10.1039/d2ra05107a

rsc.li/rsc-advances

1 Introduction

NH_3-SCR technology, the selective catalytic reduction of NO_x (NO and NO_2) to N_2 and H_2O by NH_3 with the aid of catalyst and oxygen, has become one of the main industrial deNO_x technologies due to its high efficiency and low cost.[1–4] The WO_3–V_2O_5/TiO_2 catalyst is the first commercialized NH_3-SCR catalyst since the 1970s.[5] However, WO_3–V_2O_5/TiO_2 catalysts are gradually abandoned in many countries due to their narrow temperature window (320–450 °C), poor hydrothermal stability in NH_3-SCR, and more specifically, their high biological toxicity due to the need for vanadium species.[6–8]

Cu-based and Fe-based zeolites are two potential NH_3-SCR catalysts with high catalytic activity, wide temperature window and good hydrothermal stability.[8–11] By delicately adjusting the content and distribution of metal species,[12,13] and by delicately selecting the type of support zeolites,[10,14] a variety of highly efficient Cu or Fe-based NH_3-SCR zeolite catalysts have been developed, such as Fe/SSZ-13, Fe/Beta, Fe/ZSM-5, Cu/SSZ-13, Cu/SAPO-34, and Cu/LTA zeolites.[15,16] Especially, small-pore Cu/SSZ-13 has been successfully applied in exhaust removal for diesel vehicles, though it still suffers from poor hydrothermal stability and poor sulfur resistance.[16,17]

Generally, the excellent redox properties and strong acidity are two crucial factors deciding the catalytic performance of a catalyst in NH_3-SCR.[15,16,18,19] The acid sites in catalysts facilitate the adsorption and activation of NH_3 molecules, while the redox ability of catalysts originating from metal species mainly catalyze the redox cycle in NH_3-SCR.[2] According to previous researches,[13,20–24] various Fe or Cu species existed in Fe-based or Cu-based zeolites due to the similar formation energy of metal species or the easy interconversion of different metal species under SCR reaction conditions. Therefore, it is important to reveal the catalytic roles of different active metal species in zeolites, so as to clarify the reaction mechanism of NH_3-SCR over metal-based zeolites.

According to Gao *et al.*,[13] there were mainly four kinds of iron species on Fe/SSZ-13 zeolites: isolated Fe^{2+} species, isolated Fe^{3+} species, dinuclear Fe^{3+} species ($[HO–Fe–O–Fe–OH]^{2+}$), and multinuclear Fe_xO_y species which consist of trinuclear and highly aggregated Fe_xO_y species or nanoparticles. Based on detailed investigation on Fe/SSZ-13 zeolites, Gao *et al.*[13,24] found that isolated Fe^{3+} species and dinuclear $[HO–Fe–O–Fe–OH]^{2+}$ species were the dominant active sites at low-temperature (<300 °C) and high-temperature (≥300 °C) ranges for standard NH_3-SCR, respectively, though the $[HO–Fe–O–Fe–OH]^{2+}$ species could also catalyze the undesirable ammonia oxidation side reaction. Besides, isolated Fe^{2+} species had almost no NH_3-SCR activity because of their low redox ability. In addition, the highly aggregated Fe_xO_y species in Fe/SSZ-13 zeolites, which catalyzed the ammonia oxidation side reactions, showed limited NH_3-

[a]Key Laboratory of Hubei Province for Coal Conversion and New Carbon Materials, School of Chemistry and Chemical Engineering, Wuhan University of Science and Technology, Wuhan, 430081, China. E-mail: chenjiialing@wust.edu.cn; wuxiaoqin@wust.edu.cn; Tel: +86 027 68862335

[b]School of Chemical Engineering and Pharmacy, Wuhan Institute of Technology, Wuhan, 430205, China. E-mail: ltingyu2006@126.com

[c]Hubei Key Laboratory for Processing and Application of Catalytic Materials, School of Chemistry and Chemical Engineering, Huanggang Normal University, Huanggang, 438000, China

SCR activity even at high temperatures. As a summary, isolated Fe^{3+} and dinuclear $[HO–Fe–O–Fe–OH]^{2+}$ possess excellent catalytic activity in NH_3-SCR, while isolated Fe^{2+} species, and highly aggregated Fe_xO_y species are undesirable for NH_3-SCR.[13,24]

Similar to Fe-based zeolites, several types of Cu species such as isolated Cu^+ species, isolated Cu^{2+} species (including Cu^{2+}–2Z and $[Cu(OH)]^+$–Z species, where Z represents zeolite), Cu^{2+} dimer species (including single O-bridged dicopper $[Cu–O–Cu]^{2+}$, double O-bridged dicopper or even bis(μ-hydroxo)-dicopper species), and multinuclear CuO_x species or highly aggregated CuO_x nanoparticles, can also be observed in Cu-based zeolites, according to previous researches.[4,12,25–28]

In general, researchers believed that isolated Cu^{2+} species were the main active sites for NH_3-SCR reactions over Cu-based zeolites.[12,20,25,26] Xue *et al.*[29] had observed a positive correlation between the concentration of isolated Cu^{2+} species in Cu/SAPO-34 and the NO_x conversion, and further proved that the turnover frequency (TOF) of isolated Cu^{2+} species in Cu/SAPO-34 remained almost unchanged with Cu loadings at 100–200 °C in NH_3-SCR, which strongly proved that isolated Cu^{2+} species were the main active sites in NH_3-SCR. Moreover, Gao *et al.*[27] and Paolucci *et al.*[30] found that both Cu^{2+}–2Z and $[Cu(OH)]^+$–Z species were the main active sites for standard NH_3-SCR reactions in Cu/SSZ-13, but Cu^{2+}–2Z species was more stable than $[Cu(OH)]^+$–Z species, as the latter could be easily transformed into CuO_x species under hydrothermal aging conditions.

Furthermore, researchers found that dimeric Cu^{2+} species could also be the main active species for NH_3-SCR. Gao *et al.*[12] revealed that at low temperatures (<250 °C), the standard NH_3-SCR reaction rate was positively correlated with the square of Cu loadings over Cu/SSZ-13 zeolites, which confirmed the high NH_3-SCR activity of dimeric Cu^{2+} species in NH_3-SCR at low temperatures. However, the unstable dimeric Cu^{2+} species could be converted to isolated Cu^{2+} species at high temperatures, which became the main active sites for NH_3-SCR at high temperatures. Recently, many studies revealed that Cu^+ species in Cu-based zeolites also played important roles in NH_3-SCR, especially at low temperatures.[4,29,31,32] McEwen *et al.*[28] found that both Cu^{2+} and Cu^+ species existed and participated in Cu/SSZ-13 zeolites during the NH_3-SCR reactions based on *in situ* X-ray absorption near edge spectra (XANES). Zhao *et al.*[33] also found that the active species of NH_3-SCR over Cu–Mn/SAPO-34 zeolites were a mixture of Cu^+ and Cu^{2+} species. Chen *et al.*[31] revealed that the formation of highly stable Cu^+ species in Cu/SSZ-13 was favorable for low-temperature (<200 °C) NH_3-SCR reactions.

In conclusion, different kinds of metal species had different redox ability, stability and coordination interactions with zeolite framework, which made them function differently in catalyzing NH_3-SCR reactions. However, the coexistence of various Fe species over Fe-based zeolites (or various Cu species over Cu-based zeolites) made the investigation of NH_3-SCR reactions mechanism difficult.[12] In order to suppress the occurrence of side reactions so as to investigate the detailed reaction pathway of NH_3-SCR, the total metal loadings in Cu-based or Fe-based zeolites are usually lower than 5 wt%, normally at about 2 wt%, to suppress the formation of undesired highly aggregated metal oxides or nanoparticles.[13,34,35] This poses a problem that, the qualitative and quantitative determination of various metal species over zeolites became difficult due to their low content and high dispersion over zeolites. Therefore, the detailed study on the type, content and distribution of active metal species in metal-based zeolites and their catalytic roles in NH_3-SCR with advanced characterization methods are necessary for a better understanding of NH_3-SCR reaction mechanism.

In the past 3 years, the studies of NH_3-SCR over metal oxides or metal-based zeolites were comprehensively reviewed, which mainly emphasized on the design of catalysts, reaction mechanism and deactivation mechanism. In 2019, Han *et al.*[2] published a comprehensive review on the application of metal oxide catalysts, acidic compound catalysts, metal-based zeolite catalysts, monolith catalysts and their reaction mechanism in NH_3-SCR. In addition, because of superior activity and hydrothermal stability in NH_3-SCR, many reviews were concentrated on the application of Cu-based zeolite catalysts,[36] especially in Cu-SAPO-34,[37] Cu-CHA[38,39] and Cu-based small-pore zeolites.[3,15,40] Besides, several reviews also gave detail information about the design and reaction mechanism of Fe-based zeolites for NH_3-SCR.[14,18,41,42] Besides, Andana *et al.*[43] summarized the recent research progress on the hybrid metal oxide-zeolite catalysts for low-temperature NH_3-SCR, which could enable the *in situ* NO oxidation over metal oxide and subsequently fast SCR over zeolite component through the "bifunctional mechanism".

For metal-based catalysts, many reviews focused on Mn-based oxides catalysts,[44–47] Ce-based oxides catalysts,[48] Fe-based oxides[49] and the CeO_x–MnO_x mixture catalysts[50] were published as those catalysts exhibited excellent low-temperature (<100 °C) in NH_3-SCR. In addition, the latest progress on the vanadia-based and vanadia-free metal oxides catalysts had also been summarized.[49,51] The deactivation mechanism of catalysts in NH_3-SCR and corresponding strategies to enhance the poison-resistance of catalysts were also been summarized by researchers.[19,52–55] The application of Density functional theory (DFT) in NH_3-SCR were reviewed by Guan *et al.*[56] to give clues on the mechanism studies. The influences of spatial confined structure on the catalytic performances of porous metal oxides, metal-based zeolite and metal organic framework catalysts were reviewed by Li *et al.*[57] to give new insights for the designing of future NH_3-SCR catalysts.

Though many reviews were published for NH_3-SCR, reviews about the characterization methods dealing with the determination of active metal species in Cu-based or Fe-based zeolites for NH_3-SCR are scare. Therefore, this review systematically introduced several applicable characterization methods for the accurate determination of active metal sites over Cu-based and Fe-based zeolites in NH_3-SCR, such as UV-vis absorption spectra (UV-vis), temperature-programmed reduction with H_2 (H_2-TPR), X-ray photoelectron spectroscopy (XPS), X-ray absorption fine structure spectrum (XAFS), infrared spectroscopy (IR), electron paramagnetic resonance (EPR), Mössbauer spectroscopy and DFT calculations. In addition, the applications and limitations of different characterization methods in determining Cu-based or Fe-based zeolites are also compared and summarized. The

investigation of NH_3-SCR reaction mechanism based on the above characterization methods are also introduced, hoping to shed some light on the study of NH_3-SCR mechanism over metal-based zeolites.

2 Characterization method of Cu-based or Fe-based zeolites for NH_3-SCR

2.1 UV-vis

UV-vis absorption spectroscopy (UV-vis) is one of the powerful methods to determine the chemical state and content of metal species in zeolites.[20] For example, the existence of isolated Fe^{3+} species in tetrahedral or octahedral coordination, oligomeric Fe_xO_y species, and hematite-type Fe_2O_3 species can be qualitatively determined by the characteristic absorption band of UV-vis spectra.[58] According to literature,[34,59,60] for Fe-based zeolites, the absorption band with wavelength lower than 300 nm in UV-vis spectra can be attributed to the isolated Fe^{3+} species, among which the UV absorption peak at 220–250 nm belongs to the four-coordinated isolated Fe^{3+} species while those at 250–300 nm are related to isolated Fe^{3+} species with higher coordination number such as octahedral-coordinated Fe^{3+} species. In addition, the absorption band at 300–400 nm is usually assigned to the charge transition peak of octahedral coordination aggregated Fe^{3+} species such as small Fe_xO_y species, while those with wavelength larger than 400 nm belongs to Fe_2O_3 nanoparticles. Based on the above assignments, the relative content of various Fe^{3+} species in zeolites can be estimated by the deconvolution of UV bands.[34]

Generally, for the UV-vis spectra of Cu-based zeolites, the absorption peak at about 210 and 280 nm can be attributed to charge transfer from lattice O^{2-} to Cu^{2+}, the UV band at *ca.* 750 nm is related to the d–d transitions of Cu^{2+} species with distorted octahedral coordination, all of those bands are characteristic bands of isolated Cu^{2+} species.[61–64] In addition, the absorption bands at *ca.* 250 nm and 450 nm can be assigned to CuO_x species which are caused by the charge transfer and d–d transition of octahedral coordinated Cu^{2+} in CuO_x species.[25,61,62,65] Similarly, the quantitative estimation of various Cu species can be achieved based on the above assignments, though the wavelengths of the same type of Cu species over different zeolites slightly change due to different interactions between Cu cations with zeolite framework.[62–64]

UV-vis spectroscopy conducting *in situ* is a powerful tool to provide information on the NH_3-SCR mechanism of catalysts. Zhang *et al.*[20] studied the NH_3-SCR mechanism of two active Cu species, *i.e.*, isolated Cu^{2+} and $[Cu(OH)]^+$ species, in Cu/SSZ-13 by *in situ* UV-vis with the aid of DFT calculations. They assigned the UV-vis band at 215 nm, 240 nm and 355 nm to $[Cu(OH)]^+$ species, isolated Cu^{2+} and dimer $[Cu_2O_2]^{2+}$ species, respectively, and found that two isolated $[Cu(OH)]^+$ species could bridge to form a transient $[Cu_2O_2]^{2+}$ species upon O_2 activation, while isolated Cu^{2+} species remained unchanged. In addition, the $[Cu(OH)]^+$ species exhibited stronger activity than isolated Cu^{2+} species during both reduction by NH_3 and NO oxidation reactions. Moreover, the $[Cu_2O_2]^{2+}$ intermediates could be detected under low-temperature SCR conditions. Those results indicated that $[Cu(OH)]^+$ species might play a more important role than isolated Cu^{2+} species in Cu/SSZ-13 for NH_3-SCR at low temperatures.

UV-vis spectra in combination with other techniques such as EPR, ICP-AES (inductively coupled plasma atomic emission spectroscopy) is an effective way to estimate the distribution of different metal species in zeolites.[20,35,66] However, the estimation of the fraction for various Fe species or Cu species based on the deconvolution of UV-vis spectra is only a semiquantitative method due to the unknown extinction coefficients of different adsorption band currently.[59] Meanwhile, only Fe^{3+} and Cu^{2+} species can be observed by UV-vis spectra, Fe^{2+} and Cu^+ species existing in zeolites are invisible in the wavelength range of 200–

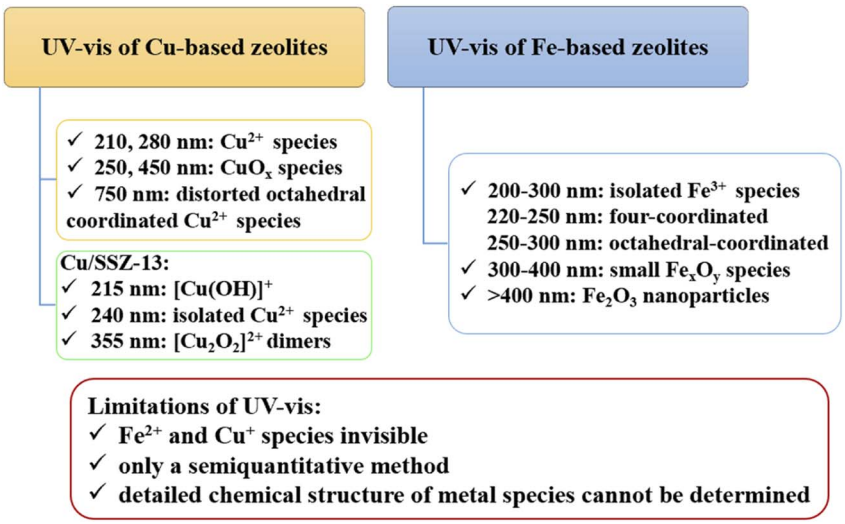

Fig. 1 Summary on the determination of Cu or Fe species in zeolites by UV-vis spectra.

Table 1 The reduction process of Cu-based or Fe-based zeolites in H_2-TPR experiments

Zeolite	Reduction steps	Ref.
Cu-based zeolites	Two step reduction of isolated Cu^{2+} species: Cu^{2+} to Cu^{+}: ~400 °C; Cu^{+} to Cu^{0}: 700–900 °C	27, 29, 74 and 77
	Two step reduction of $[Cu(OH)]^{+}$ species: $[Cu(OH)]^{+}$ to Cu^{+}: ~250 °C; Cu^{+} to Cu^{0}: 360 °C	27, 74 and 77
	Directly reduction of CuO to Cu^{0}: ~300 °C	27, 29 and 74
Fe-based zeolites (reduction temperature increases with Fe_xO_y particle size)	Two step reduction of isolated Fe^{3+} species: Fe^{3+} to Fe^{2+}: 380–430 °C; Fe^{2+} to Fe^{0}: 900–1000 °C	69, 71 and 72
	Reduction of small Fe_xO_y species: 500–560 °C	24, 69 and 70–72
	Reduction of large Fe_2O_3 nanoparticles: 680–750 °C	24, 69 and 70–72
	Reduction of aggregated Fe_2O_3 or Fe_3O_4 particles: >1000 °C	34 and 73

800 nm in UV-vis experiments (for example, the adsorption band of Fe^{2+} species is located in the near infrared range around 1000 nm (ref. 66)). Moreover, only the coordination state of metal species can be obtained from UV-vis spectra, the detailed chemical structure, for example, whether the tetrahedral coordinated Cu^{2+} or Fe^{3+} species are in the framework or extra-framework of zeolites cannot be distinguished.[64,67] Therefore, the accurate determination of metal species in zeolites by UV-vis should be available with the aid of other methods, such as EPR, ICP-AES, H_2-TPR and IR experiments. In conclusion, the application and determination of Cu or Fe species in zeolites for NH_3-SCR by UV-vis are summarized in Fig. 1.

2.2 H_2-TPR

Temperature-programmed reduction with H_2 (H_2-TPR) is a widely used method to differentiate chemical valence of Cu or Fe species in zeolites by the reduction reaction between hydrogen and metal cations. The reduction temperature can be used to distinguish the chemical valence of metal species, while the deconvoluted reduction peak area in the H_2-TPR profiles can be used to estimate the content of metal species.[27,68]

The reduction process of Fe-based zeolites are quite complex, as various kinds of Fe species such as isolated Fe^{3+} species, Fe^{2+} species, Fe_xO_y clusters, large Fe_2O_3 nanoparticles can be easily formed in zeolites due to their similar energy of formation.[13] However, by summarizing previous literature,[24,69,70] the reduction peak of different Fe species can be roughly divided into several temperature ranges. The reduction of isolated Fe^{3+} at the ion-exchange sites of zeolites to Fe^{2+} are usually occurred at 380–430 °C, while the further reduction of these Fe^{2+} species to Fe^{0} can only take place at about 900–1000 °C due to the strong electrostatic interactions between Fe cations and the O–Al sites of zeolites.[69,71,72] In addition, the reduction temperature of iron oxide clusters increases with their particle size, according to Brandenberger *et al.*[69] Generally, the reduction of small Fe_xO_y clusters and large Fe_2O_3 nanoparticles are in the temperature range of 500–560 °C and 680–750 °C, respectively. In addition, some highly aggregated Fe_2O_3 or Fe_3O_4 particles are hard to be reduced during the H_2-TPR experiments. Those Fe species can be reduced only by increasing the reduction temperatures to about 1000 °C, which usually causes the collapse of zeolite framework.[34,73]

For Cu-based zeolites, the reduction of isolated Cu^{2+} species at the ion-exchange sites of zeolites usually undergo two steps:[27,29,74–76] the reduction of Cu^{2+} to Cu^{+}, and further to Cu^{0}. The reduction of two kinds of isolated Cu^{2+} species, *i.e.*, Cu^{2+}–2Z and $[Cu(OH)]^{+}$–Z (Z represents zeolite) happen at different temperatures due to their different stability in zeolites:[27,74,77] the reduction of more stable Cu^{2+}–2Z to Cu^{+} happens at about 400 °C, while that of less stable $[Cu(OH)]^{+}$–Z species at about 250 °C with a further reduction peak of Cu^{+} to Cu^{0} at about 360 °C. The reduction of CuO nanoparticles in Cu-based zeolites are much easier than Cu cations. CuO nanoparticles could be directly reduced to Cu^{0} by hydrogen at around 300 °C.[27,29,74] Occasionally, reduction peak at around 700–900 °C emerged at the H_2-TPR profiles of Cu-based zeolites, which could be attributed to the reduction of Cu^{+} at the ion-exchange sites of zeolites to Cu^{0} process, as the strong interactions between zeolite framework and Cu^{+} species hindered the reduction process.[27,29] Table 1 summarizes the reduction steps of Cu-based or Fe-based zeolites by H_2-TPR experiments.

Calculating the H_2 consumption of each reduction peak by deconvolution the H_2-TPR profiles is an effective way to quantitatively estimate the content of various metal species in zeolites. The reduction process of different kinds of Cu species in Cu-based zeolites are shown in formula (1)–(4). Combining the reduction temperatures and H_2 consumption of various Cu species in H_2-TPR profiles, the content of various Cu species in Cu-based zeolites could be roughly estimated, according to previous literature.[77–79]

$$Cu^{2+} + \frac{1}{2}H_2 \rightarrow Cu^{+} + H^{+} \quad (H_2/Cu = 0.5) \tag{1}$$

$$[Cu(OH)]^{+} + \frac{1}{2}H_2 \rightarrow Cu^{+} + H_2O \quad (H_2/Cu = 0.5) \tag{2}$$

$$Cu^{+} + \frac{1}{2}H_2 \rightarrow Cu^{0} + H^{+} \quad (H_2/Cu = 0.5) \tag{3}$$

$$Cu^{2+} + H_2 \rightarrow Cu^{0} + 2H^{+} \quad (H_2/Cu = 1) \tag{4}$$

By conducting H_2-TPR experiments, Gao *et al.*[77] had semi-quantitively determined the isolated Cu^{2+} and $[Cu(OH)]^+$ species and excluded the existence of CuO aggregated species in Cu/SSZ-13. Further, by combing with EPR and NH_3-SCR kinetic experiments, they investigated the influences of Si/Al ratio and Cu content in Cu/SSZ-13 on the NH_3-SCR mechanism and found that the six-membered rings (6MR) faces with 2 Al atoms in the CHA structure were the most favorable site in stabilizing Cu^{2+} ions, while Cu^+ and $[Cu(OH)]^+$ became the most stable Cu species in the absence of 2 Al sites. Song *et al.*[27] also distinguished Cu^{2+} and $[Cu(OH)]^+$ in Cu/SSZ-13 by H_2-TPR and further studied the hydrothermal stability of them in NH_3-SCR by combining EPR, DFT and kinetic reactions. They found that isolated Cu^{2+} species exhibited higher stability than $[Cu(OH)]^+$ under hydrothermal aging conditions, which provided the atomic-level understanding of transformation of Cu species in NH_3-SCR. Those literature indicate that H_2-TPR is also an effective tool for the investigation of NH_3-SCR mechanism.

However, when H_2-TPR is used for the determination of metal species in zeolites, there are certain limitations: the reduction temperature of H_2-TPR is usually below 1000 °C, so it is incapable to effectively detect the metal species that are extremely difficult to reduce.[34] Moreover, the H_2-TPR experiments cannot detect the zero valent metals in the zeolites. Furthermore, though H_2-TPR can be used to determine both Cu^+ and Cu^{2+} or Fe^{2+} and Fe^{3+} species in Cu-based or Fe-based zeolites, the reduction peak could be affected by many factors.

Firstly, the differentiation of reduction peaks for various metal species in zeolites are sometimes difficult, as the reduction peak of the same type of metal species usually shift with the zeolite supports and preparation method. For example, the reduction temperature of Cu species in zeolites slightly changed when using different zeolites as support, as the reduction behaviors of metal species were sensitive to the zeolite support and local chemical environment of metal species.[62,75,78,80] Secondly, the reduction temperature of metal species may also shift with the increasing of metal content, as the gradually formation of aggregation metal species may be undetectable in H_2-TPR or the overlapped reduction peaks may form a large broad peak.[35] Thirdly, the H_2O molecules adsorbed on the metal-based zeolites also affect the determination of H_2-TPR, as the dehydration process of metal-based zeolites before the H_2-TPR experiments can cause the auto-reduction of metal species which eventually decrease the H_2 consumption in the H_2-TPR profiles.[77,81] Lastly, the shape and area of reduction peak in the H_2-TPR experiments could also be affected by the heating rate of temperature-programmed process.[82] Therefore, when H_2-TPR is used to detect active metals on zeolites, it is necessary to select reasonable and repeatable experimental conditions, be careful in qualitative and quantitative analysis of H_2-TPR results, and combine with other characterization methods to ensure the accuracy of the results.

2.3 XPS

X-ray photoelectron spectroscopy (XPS) based on photoelectric effect equation is often used to determine the composition and chemical valence of elements on zeolite catalysts by exciting the inner electrons and measuring the binding energy of elements.[83]

The XPS signal of Cu 2p in Cu-based zeolites are usually separated into Cu $2p_{3/2}$ and Cu $2p_{1/2}$ doublet structures (two peaks) due to the spin–orbit coupling. Generally, the Cu^+ $2p_{3/2}$ and $2p_{1/2}$ signals are located at binding energy of *ca.* 932.5 ± 0.2 eV and 952.3 ± 0.2 eV, respectively, while Cu^{2+} $2p_{3/2}$ and $2p_{1/2}$ signals are located at about 933.7 ± 0.2 eV and 953.6 ± 0.2 eV, respectively.[84,85] In addition, the satellite peak at about 944 eV is also characteristic of Cu^{2+} species. However, the shift of binding energy for the same kind of Cu species are usually observed by many researchers, as the coordination structure and chemical state of Cu species can be significantly affected by the Cu loadings, preparation method and the zeolite supported of Cu-based zeolites. Xu and co-workers[86] had observed the Cu^{2+} $2p_{2/3}$ and $2p_{1/2}$ signals at about 935.2 eV and 955.0 eV on Cu/Beta zeolites, which were related to the special local structure of Cu^{2+} species between Cu species and BEA framework. Moreover, previous researchers had different assignments for the binding energy at 928–940 eV of Cu $2p_{3/2}$ structure in Cu-based zeolites. Han and co-workers[87] assigned the two asymmetric signals at 933.5 eV and 936.5 eV to CuO species and isolated Cu^{2+} species in Cu/SSZ-13, which were supported by the Auger electron spectra and many other researchers.[88–90] Therefore, the distinguish of Cu^+ and Cu^{2+} species are not easy by XPS method, as the chemical state of Cu species are related to the support, which should be analyzed by combining several types of characterization methods.[91]

Similar to Cu 2p spectra, the XPS signal of Fe 2p spectra are also split into Fe $2p_{3/2}$ and Fe $2p_{1/2}$ doublet structures due to the spin–orbit coupling.[84,92–94] Unlike Cu 2p spectra, the assignment of Fe 2p spectra are relatively clear, though slight shift of binding energy for different catalysts.[92,94,95] Generally, the Fe^{2+} $2p_{3/2}$ and $2p_{1/2}$ signals are located at binding energy of *ca.* 710 eV and 723 eV with satellite peaks at *ca.* 715 eV and 729 eV, respectively, while Fe^{3+} $2p_{3/2}$ and $2p_{1/2}$ signals are located at about 711 eV and 724 eV with satellite peaks at *ca.* 719 eV and 733 eV, respectively.[92,96] According to the above assignments, researcher had estimated the relative content of Fe^{3+} and Fe^{2+} species over Fe/Beta, Fe/ZSM-5 and Fe/MOR zeolites, which was in accordance with ^{57}Fe Mössbauer spectra results.[96]

Based on XPS results of catalysts before and after hydrothermal aging treatment, Lee *et al.*[83] confirmed the formation of $CuAl_2O_4$ species (935 eV) in Cu/SSZ-13, Cu/UZM-35, Cu/Beta, Cu/ZSM-5 zeolites during the hydrothermal aging process, by combing with H_2-TPR, UV-vis and XANES experiments. They found that the extent of transformation of isolated Cu^{2+} species into CuO_x and $CuAl_2O_4$ species during hydrothermal aging process was higher in the order of Cu/SSZ-13 < Cu/UZM-35 < Cu/Beta < Cu/ZSM-5, which was in line with the higher stability of Cu/SSZ-13 and Cu/UZM-35 than Cu/Beta and Cu/ZSM-5 in NH_3-SCR. Xu *et al.*[86] had compared the NH_3-SCR activity of copper and iron bimetal modified Beta zeolite (Cu–Fe/Beta) with that of Cu/Beta and Fe/Beta mono-component Beta zeolites and found that Cu–Fe/Beta exhibited higher low-temperature activity and wider temperature window than the rest two zeolites. Based on

Table 2 The typical attribution of XPS signals in Cu-based or Fe-based zeolites

	Attribution of XPS signals	Ref.
Cu-based zeolites	Characteristic of Cu^+ species: Cu^+ $2p_{3/2}$: ~932.5 eV; Cu^+ $2p_{1/2}$: ~952.3 eV, shift to 935.2 eV and 955.0 eV in Cu/Beta	84–86
	Characteristic of Cu^{2+} species: Cu^{2+} $2p_{3/2}$: ~933.7 eV; Cu^{2+} $2p_{1/2}$: ~953.6 eV; satellite peak: ~944 eV	84 and 85
	Different attributions in Cu/SSZ-13: CuO: 933.5 eV; isolated Cu^{2+} species: 936.5 eV	87
	$Cu_2Al_2O_4$: ~935 eV	83
Fe-based zeolites	Characteristic of Fe^{2+} species: Fe^{2+} $2p_{3/2}$: ~710 eV; Fe^{2+} $2p_{1/2}$: ~723 eV; satellite peaks: ~715 eV and 729 eV	92 and 94–96
	Characteristic of Fe^{3+} species: Fe^{3+} $2p_{3/2}$: ~711 eV; Fe^{3+} $2p_{1/2}$: ~724 eV satellite peaks: ~719 eV and 733 eV	92 and 94–96

XPS measurement, they revealed that the dispersion state of active components and the ratios of Cu^{2+}/Cu^+ and Fe^{3+}/Fe^{2+} in the Cu–Fe/Beta zeolite were increased when comparing with the other two zeolites due to the synergistic effect of copper and iron species, which was also supported by XRD, UV-vis and EPR results. Based on above researches, Table 2 summarizes the attribution of XPS signals in Cu-based or Fe-based zeolites.

Thought XPS can distinguish various Fe or Cu species by nondestructive testing which only need small amounts of sample (10–50 mg for zeolites), it can only detect elements of nanoscale thickness on the surface of zeolites, while the accurate determination of composition of the whole zeolites required element analysis by ICP-AES method.[84,97,98] In addition, the automatic reduction of Cu^{2+} to Cu^+ (or Fe^{3+} to Fe^{2+}) species was sometimes inevitable due to the ultra-high vacuum conditions of XPS determination, which would cause the deviation of XPS testing results from the actual state of zeolites.[99] Moreover, the binding energy of metal species may shift with zeolite supports due to the different interactions between metal species and zeolite framework.[89,96] Therefore, the accurate analysis of various metal species by XPS should take the above factors into account and often needs to be carried out by combining other characterization methods such as ICP-AES, EPR, Auger electron spectra and UV-vis spectra.[83,90,93,97,100]

2.4 XAFS

The X-ray absorption fine structure spectroscopy (XAFS) is an atomic-scale tool to study the local structure and chemical state of metal species in zeolites.[101–103] When the energy of X-ray resonates with the ionization energy of the inner layer electron of atoms, the electron is excited to form a continuous spectrum (XAFS). The X-ray absorption near-edge structure (XANES) consists of the regime from −10 eV below to *ca.* 50 eV above the edge energy E_0, which can be used to determine the electronic state of the absorbing atom, such as oxidation number and the geometric structure.[104] The extended X-ray absorption fine structures (EXAFS) comprises the regime from about 50 eV to about 1000 eV above E_0, which can be used to determine the local structure of atoms, as EXAFS can provide the interatomic distances and coordination numbers for several coordination shells around the absorbing atom.[104]

In recent years, XAFS has been widely used to study the active sites of metal-based zeolites in NH_3-SCR reactions. Deka *et al.*[26] had studied the local environment of copper species in Cu/SSZ-13 under realistic NH_3-SCR conditions by *in situ* XAFS and *in situ* XRD experiments, and confirmed that the isolated Cu^{2+} species located in the double-six-ring (D6R) subunit of CHA structure were the main active sites for NH_3-SCR. In addition, they found that the isolated Cu^{2+} species suffered from a conformational change in the local geometry from a planar form to a distorted tetrahedron due to a preferential interaction with NH_3 at low temperatures, which process resulted in the stymieing of activity. In contrast, due to the weak interactions between the isolated Cu^{2+} species and NH_3, the local structure of isolated Cu^{2+} species remained unchanged at high temperatures, which results in the high activity of Cu/SSZ-13 in NH_3-SCR. Korhonen *et al.*[25] also found that isolated Cu^{2+} species were the main active sites in NH_3-SCR over Cu/SSZ-13 zeolites based on EXAFS experiments.

McEwen *et al.*[28] had explored the Cu oxidation state and coordination environment in Cu/SSZ-13 zeolites during the NH_3-SCR reactions by *operando* XAFS experiments and found that, tetrahedral coordinated Cu^{2+} species dominated in Cu/SSZ-13 under fast NH_3-SCR ($NO_2/NO_x = 0.5$) and NO_2-SCR ($NO_2/NO_x = 1$) reaction conditions, while both Cu^+ and Cu^{2+} species existed in Cu/SSZ-13 zeolite under standard NH_3-SCR ($NO_2/NO_x = 0$) reaction conditions, which indicated that partial reduction of copper species occurred under the standard NH_3-SCR atmosphere. As shown in Fig. 2, Lomachenko *et al.*[105] had monitored the oxidation state, mobility of Cu species over Cu-CHA zeolites during NH_3-SCR reactions at 150–400 °C range by *operando* XAFS experiments and unambiguously identified two distinct regimes for the catalytic mechanism of Cu active sites. In the low temperature range (<200 °C), Cu^+ (m-Cu(I) complexes) and Cu^{2+} species (Z–Cu(II) and m-Cu(II) complexes) were the main catalytic active centers, which were solvated by

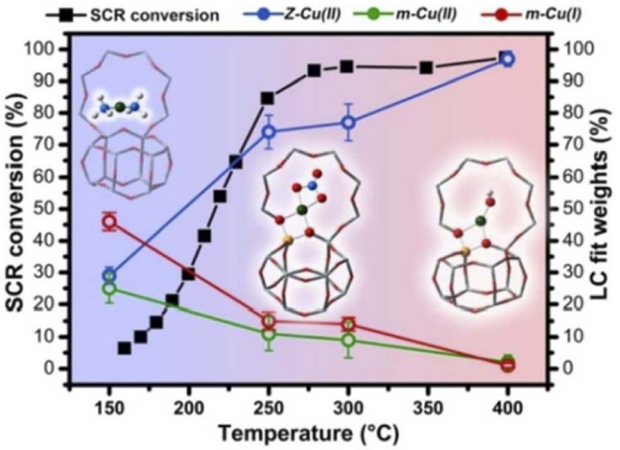

Fig. 2 The relationship between the relative percentages of Z–Cu(II), m-Cu(II) and m-Cu(I) species and the NH_3-SCR activity in different temperatures. Z–Cu(II) stands for the sum of Z–[Cu(II)OH^-] and Z–[Cu(II)NO_3^-] complexes, while m-Cu(II) represents the sum of mobile $[Cu(II)(NH_3)_4]^{2+}$ and $[Cu(II)(H_2O)_6]^{2+}$ complexes. m-Cu(I) represents the mobile $[Cu(I)(NH_3)_2]^+$ complexes in Cu/SSZ-13 zeolites (atoms color code: Cu: green, O: red, Al: yellow, Si: gray, N: blue, H: white).[105] (with permission from ACS publications).

NH_3 due to the strong coordination between NH_3 and copper species. In the middle and high temperature range (250–400 °C), the main catalytic active centers were isolated Cu^{2+} species (Z–Cu(II) complexes) which were coordinated with zeolite framework.

The detail understanding of the redox cycle of active metal species is important for the revealing of NH_3-SCR reaction mechanism, as NH_3-SCR is a redox reaction. Ueda *et al.*[106] had investigated the redox cycle of Cu species in Cu/ZSM-5 for NH_3-SCR based on *in situ* XAFS experiments. They found that Cu^{2+} species could be slowly reduced to Cu^+ species by NH_3 flow, which process could be accelerated by adding NO to the NH_3 flow. However, for the oxidation half-cycle, the complete oxidization of Cu^+ to Cu^{2+} species could only be achieved by the NO and O_2 mixture flow but oxygen alone. Those results indicated that the oxidation half-cycle of Cu^+ to Cu^{2+} process was more difficult than the reduction half-cycle, which was the rate-limiting step for the whole NH_3-SCR reactions. Further, Gao *et al.*[32] had studied the detailed pathway of the oxidation half-cycle on Cu/SSZ-13 by *in situ* EXAFS experiments combined with DFT calculations, and confirmed that for NH_3-SCR reactions at low temperatures, the oxidation half-cycle of Cu(I) to Cu(II) requires the participation of two isolated Cu^+ species by forming $[Cu^I(NH_3)_2]^+$–O_2–$[Cu^I(NH_3)_2]^+$ as intermediates.

Lercher *et al.*[107] had studied the redox process of Fe/Beta in NH_3-SCR by determining the fraction of Fe^{2+} and Fe^{3+} species through the combination of XANES and Mössbauer spectroscopy, they found that the distribution of Fe^{2+} and Fe^{3+} in Fe/BEA zeolites depended mainly on both the Fe content in zeolites and the conditions of the thermal treatment. In addition, they also revealed that the ion exchanged isolated Fe^{2+}/Fe^{3+} species are reversibly oxidized and reduced under real NH_3-SCR conditions, which were the main active sites for NH_3-SCR. Doronkin *et al.*[108] had investigated the structure of iron sites in Fe/Beta and

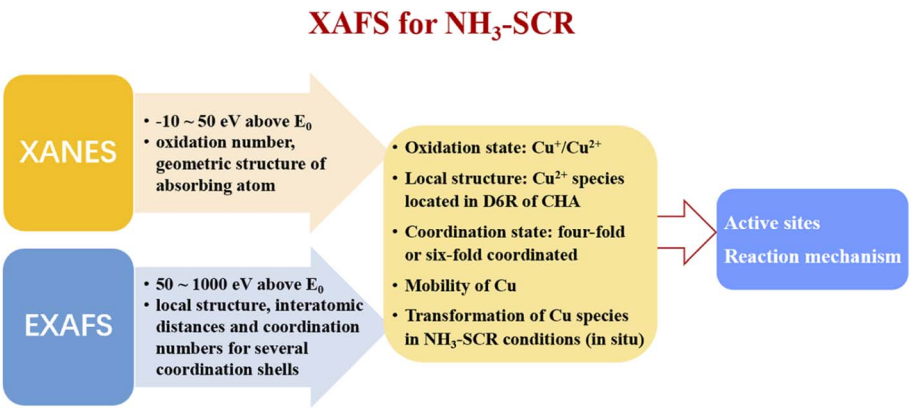

Fig. 3 Summary on the studying of NH_3-SCR mechanism in Cu/zeolite by XAFS.

Table 3 Assignment of IR bands of NO adsorption complexes in Fe/H-SSZ-13 zeolite according to Szanyi *et al.*[125] (with permission from RSC Publications)

Adsorption center	P_{NO}	Low	Medium	High
Fe^{2+} in 8 MR of CHA	Ads. complex	$Fe^{2+}(NO)$	$Fe^{2+}(NO)_2$	$Fe^{2+}(NO)_3$
	IR peak position	1900	1771	1801
				1810
			1852	1917
Fe^{2+} in 6 MR of CHA	Ads. complex	$Fe^{2+}(NO)$	$Fe^{2+}(NO)$	$Fe^{2+}(NO)$
	IR peak position	1884	1884	1884

Table 4 The assignment of IR bands after CO adsorption over several Fe-based zeolites

	FTIR bands after CO adsorption over Fe-based zeolites (cm^{-1})						
	Fe^{2+}–CO	Fe^{2+}–$(CO)_2$	OH–CO adducts	Fe^{3+}–OH···CO	Al^{3+}–CO complex	FeO_x–(CO)	Ref.
Fe/Beta	2190	—	2175	2157	2225	—	58
Fe/FER	2187, 2195 (in small cavities); 2196 (in large cavities)	2188	2173	—	—	—	122
Fe/SSZ-13	2198 (in 6 MR) 2207 (in 8 MR)	—	2175	—	2221 2231	2129 2148 2177	125

copper sites in Cu-SAPO-34 zeolites during the real NH_3-SCR conditions by *operando* spatially-resolved and time-resolved XAFS experiments, respectively. They found strong gradients of Fe and Cu oxidation state along the Fe/Beta and Cu-SAPO-34 catalyst bed, respectively. By detailed studies on the change tendency of relative percentages of Fe and Cu oxidation state in NH_3-SCR reactions over Fe/Beta and Cu-SAPO-34 catalyst, respectively, they concluded that the re-oxidation of Cu or Fe in zeolites was the rate-limiting step in NH_3-SCR. Dahl *et al.*[109] had studied the NH_3-SCR reaction mechanism over Fe-Beta zeolites by *in situ* XANES and EXAFS experiments. They also found a relation between the oxidation state of iron and the NH_3-SCR catalytic activity of Fe/Beta zeolites and concluded that isolated iron species were the active sites while the re-oxidation of iron species was one of the rate-limiting steps in NH_3-SCR.

It is worthy to note that the chemical state of Cu or Fe species in zeolites during the NH_3-SCR reactions will undergo successive reduction and oxidation steps so as to catalyze the redox process. Therefore, in most of the literature, the investigation of chemical state of the metal species in zeolites were conducted by *in situ* or *operando* XAFS under NH_3-SCR reaction conditions, so as to reveal the detail reaction mechanism of NH_3-SCR. However, the *ex situ* XAFS experiment of metal-based zeolites can still provide valuable information to NH_3-SCR mechanism. Firstly, the *ex situ* XAFS experiment can be used to determine the state of metal species in the as-prepared catalysts, supported by other characterization methods such as UV-vis, H_2-TPR, *etc.*[110] Korhonen *et al.*[25] compared the EXAFS spectra of Cu/SSZ-13 zeolites before and after calcination and found the coordination number of Cu^{2+} ions in SSZ-13 reduced from 4 to 3, along with the decrease of average distance of Cu–O distance from 2.02 Å to 1.93 Å, which indicated that the state of Cu in SSZ-13 is sensitive to reaction conditions. In addition, the good fitness of experimental EXAFS and calculated ones confirmed the validity of the proposed local structure of the isolated Cu^{2+} species in SSZ-13, which is important for the further studying of NH_3-SCR mechanism. Secondly, by comparing the *ex situ* XAFS results of catalysts treated at different gas and temperature conditions, it is possible to speculate the reaction mechanism of catalysts in NH_3-SCR. Deka *et al.*[26] had studied the Cu K-edge XANES spectra of Cu-SSZ-13 after calcination and under NH_3-SCR conditions at different temperatures (125–300 °C). They found that the local environment of isolated Cu^{2+} species (located on the plane and slightly distorted from the center of the D6R subunits of CHA) under NH_3-SCR reaction at 300 °C was similar to that seen after calcination, whereas a conformational change from a square planar to a distorted tetrahedral type structure was observed for isolated Cu^{2+} species at 125 °C in NH_3-SCR conditions due to a direct interaction of NH_3 with copper, according to XANES and EXAFS spectra results. Those results indicated that the reaction mechanism of Cu-SSZ-13 in NH_3-SCR changed with reaction temperatures, which was further confirmed by Lomachenko *et al.*[111] through *operando* XAFS and Emission Spectroscopies. In conclusion, the application of XAFS over Cu-based zeolites for investigating NH_3-SCR mechanism is summarized in Fig. 3.

The fine structures at X-ray absorption edges contain information about the geometrical and electronic structure of

Table 5 The assignment of FTIR bands after CO adsorption over several Cu-based zeolites

	FTIR bands after CO adsorption over Cu-based zeolites (cm^{-1})								
Zeolite	Cu^+–CO	Cu^+–$(CO)_2$	Cu^+–$(CO)_3$	Cu^{2+}–CO	OH^-–CO	$[Cu(OH)]^+$···CO	Al^{3+}···CO	CuO_x···CO	Ref.
Cu-SSZ-13	2155	2150, 2178	2134, 2169, 2194	—	—	2207	2220	—	131
Cu-SSZ-13	2158	2148	—	—	2177	—	—	—	127
Cu-SSZ-13	2135, 2154	2178	—	2220	—	—	—	—	129
Cu/SAPO-34	2154	2147, 2178	2139, 2163, 2187	—	2171	—	—	2131	127
Cu/ZSM-5	2158	2150, 2178	2134, 2166, 2192	—	—	—	—	—	131 and 132
Cu/Beta	2158, 2153	2152, 2180	2134, 2168, 2193	—	—	—	—	—	131
Cu/MOR	2159	2152, 2180	2146, 2167, 2193	—	—	—	—	—	133
Cu/FER	2157	2149, 2178	2135, 2170, 2191	—	—	—	—	—	134

absorbing atoms, which has been widely used in the study of NH_3-SCR reaction mechanism over metal-based zeolite catalysts.[101,112–114] However, the major disadvantage of XAFS experiment is that the signals of all absorbing atoms of one type in the sample may overlap at the edge, which made it difficult to distinguish the individual signals belonging to different species when the sample contains an element in several different atomic environments.[102] Another disadvantage of XAFS is that the accessibility of synchrotrons of X-ray is not easy, as beam times are scarce which need to be scheduled months ahead.[104]

2.5 FTIR spectroscopy

Infrared (IR) spectroscopy can detect the framework vibration of zeolites, the chemical bond vibration of metal cationic in zeolites and the vibration of bonds between adsorbent and zeolite framework, so as to analyze the structure of metal-based zeolites, or capture the surface adsorption groups and active intermediates on catalysts.[115–118] In NH_3-SCR, the Fourier transform infrared spectra (FTIR) after *in situ* adsorption of NO or CO (FTIR of adsorption NO or CO) are often used to explore the status of metal active species on the zeolite catalysts,[119–122] as CO and NO molecules can form coordination complexes with metal cations which can be detected by infrared spectroscopy.

The FTIR of adsorption NO or CO experiments can be used to selectively determine the Fe^{2+} species in zeolites, as the adsorption of NO or CO on Fe^{3+} are too weak to be detected.[24] Though the pre-treatments of Fe-based zeolites for FTIR experiments under high temperature and ultra-high vacuum (about 300–500 °C and 10^{-5} Pa) may cause the automatic reduction of Fe^{3+} species to Fe^{2+} species, thus bringing about the deviation of FTIR spectra from the actual one, the FTIR spectra of adsorption NO or CO can still provide key information about the catalysts.[115,123,124]

Gao *et al.*[24,125] showed that NO could coordinate with Fe^{2+} species to form a variety of Fe complexes on Fe/SSZ-13 zeolites: the mononitrosyl Fe^{2+}–NO species (1885 cm^{-1}) formed in the six-membered rings (6MR) of CHA structure, the dinitrosyl Fe^{2+}–$(NO)_2$ (1850 and 1772 cm^{-1}) and trinitrosyl Fe^{2+}–$(NO)_3$ (1916, 1810 and 1797 cm^{-1}) species formed in the eight-membered ring (8MR) windows of CHA cage. By comparing the chemical statues and content of Fe^{2+} species before and after hydrothermal aging treatments, the migration and transformation behaviors of Fe^{2+} species in Fe/SSZ-13 zeolites were also clarified by Gao *et al.*,[24] which suggested that even hydrothermal aging at 600 °C could result in the aggregation of Fe^{2+} species and the formation of $FeAlO_x$ clusters with low reducibility in NH_3-SCR. Szanyi and co-workers[125] found two kinds of mononitrosyl Fe^{2+}–NO species existed in Fe/SSZ-13 zeolites by FTIR of NO adsorption experiments, one was the Fe^{2+}–NO species in the restricted environment (at the ion-exchange sites in six-membered rings of CHA structure, with FTIR signal at 1880 cm^{-1}) which were thermodynamically stable, the other was the unstable Fe^{2+}–NO species in the open environment (in the CHA cages, with FTIR signal at 1900 cm^{-1}), which would gradually transform into trinitrosyl Fe^{2+}–$(NO)_3$ complex, as supported by the shift of infrared absorption band to 1800–1830 cm^{-1}. According to Szanyi *et al.*,[125] the assignment of FTIR bands after NO adsorption over Fe-based H-SSZ-13 zeolites are summarized in Table 3. The Fe^{2+} species located in the eight-membered ring (8MR) of the large CHA cage could form three types of Fe^{2+}–$(NO)_x$ species with NO (*i.e.*, Fe^{2+}–NO, Fe^{2+}–$(NO)_2$ and Fe^{2+}–$(NO)_3$) by increasing the adsorption pressure of NO, whereas only mononitrosyl Fe^{2+}–NO species could be formed in Fe^{2+} species located in the six-membered rings (6MR) of double six-member (D6R) prisms due to the strong electrostatic interactions between Fe^{2+} ions and zeolite framework.

CO is a sensitive probe for the characterization of Fe^{2+} species over zeolites. Kim and co-workers[58] had investigated the distribution of Fe species on Fe/Beta zeolites by IR spectroscopy of adsorbed CO, they found that the primary bands at 2190, 2175 and 2157 cm^{-1} were attributed to Fe^{2+}–CO species, the acidic OH–CO adducts and to CO interacting with Fe^{3+}–OH species, respectively, as the direct interactions between Fe^{3+} and CO were too weak to form Fe^{3+}–CO species.[126] In addition, the weak bands at about 2225 cm^{-1} and 2130 cm^{-1} were attributed to Al^{3+}–CO complex and physiosorbed CO, respectively. Moreover, by introducing O_2 onto the surface of Fe/Beta zeolites, the fraction of Fe^{2+} species (reflecting by the Fe^{2+}–CO bands at 2190 cm^{-1}) apparently decreased correspondingly with the dramatically increasing of Fe^{3+} species (representing by the Fe^{3+}–OH$\cdots$CO band at 2157 cm^{-1}), which suggested the oxidation of Fe^{2+} species to Fe^{3+} species in the presence of O_2 over Fe/Beta zeolites. Malpartida and co-workers[122] also found that CO could distinguish two kinds of Fe^{2+} species in Fe/FER zeolites by IR spectroscopy of adsorbed CO under dynamic vacuum: one is the mono-carbonyl Fe^{2+}–CO species (with strong bands at 2196 cm^{-1}) formed by CO with the most abundant iron sites at large cavities of ferrierite zeolites, which could be transformed to di-carbonyl species by increasing CO pressure; the other is the mono-carbonyl Fe^{2+}–CO species (with weak IR bands at 2187 cm^{-1}) formed by CO coordinating with less abundant iron sites located in more confined sites, which were more stable than the former one and couldn't be converted to di-carbonyl species. Szanyi *et al.*[125] also investigated the FTIR spectra after CO adsorption over Fe/SSZ-13 zeolites, in which several IR bands were different from the above-mentioned Fe-based zeolites, which was reasonable as the coordination environments of Fe^{2+} species in different zeolites were slightly changed. By summarizing the above literature, the assignments of IR bands after CO adsorption over several Fe-based zeolites are summarized in Table 4.

Similar to Fe-based zeolites, IR spectroscopy of adsorbed CO can be used to selectively determine the Cu^+ species in Cu-based zeolites, while the adsorption of CO on Cu^{2+} species are much weak.[127,128] According to Corma and co-workers,[127] the IR absorption band of the mono-carbonyl Cu^+–CO complex formed by CO interacting with Cu^+ at the ion exchange sites of Cu/CHA zeolites appeared at about 2155 cm^{-1}, while the absorption peak at about 2180 cm^{-1} could be attributed to the asymmetric stretching of the bicarbonyl Cu^+–$(CO)_2$ complex formed by two CO molecules with one Cu^+ species. Szanyi *et al.*[129] had studied the distribution of Cu species on Cu/SSZ-13 by IR spectroscopy and found that the adsorbed CO at room temperature primarily

Table 6 The assignment of FTIR bands after NO adsorption over several Cu-based zeolites

	FTIR bands after NO adsorption over Cu-based zeolites (cm^{-1})						
Zeolite	Cu^{+}–NO	Cu^{+}–$(NO)_2$	Cu^{2+}–NO	Cu^{2+}–$(NO)_2$	$[Cu(OH)]^{+}\cdots$ NO	$[Cu–O–Cu]^{2+}\cdots$ $(NO)_2$	Ref.
Cu/SSZ-13	1809	1826, 1728	1890	—	—	—	131
Cu/SSZ-13	1803, 1816	1663, 1800, 1654, 1783	1925, 1947, 1960, 1965, 1977	1801, 1892, 1869, 1813, 1874	1795, 1788	—	127
Cu/SAPO-34	1811, 1821	1720, 1831, 1714, 1828	1907, 1940, 1943, 1968	1809, 1888, 1802, 1868	1790, 1798	1712, 1887	127
Cu/ZSM-5	1813	1730, 1825	1921, 1912, 1905, 1895	—	—	—	131 and 135
Cu/Beta	1802, 1815	1828, 1734	1912, 1903, 1895	—	—	—	131 and 136
Cu/MOR	1813	1730, 1828 (main channel); 1785, 1870 (side pocket)	1960, 1938, 1921, 1909, 1895	—	—	—	135 and 137

formed Cu^{+}–CO species, but Cu^{+}–$(CO)_2$ and Cu^{2+}–CO species could also be formed when excessive CO were dosed.

In contrast to IR spectroscopy of CO adsorption, IR spectroscopy of NO adsorption can detect both Cu^{2+} and Cu^{+} species in Cu-based zeolites, due to the strong interactions between NO and copper cations.[127,129,130] Concepcion *et al.*[127] found that only the mono-nitroso complex Cu^{2+}–NO could be formed on Cu/SSZ-13 and Cu/SAPO-34 zeolites due to the strong coordination between isolated Cu^{2+} and framework oxygen of zeolites, which exhibited two IR bands at around 1925 cm^{-1} and 1950 cm^{-1}, attributing to two kinds of Cu^{2+}–NO complexes formed by NO reacting with Cu^{2+} species located in the six-membered and eight-membered rings of CHA structures, respectively. In contrast, various nitro complexes could be formed between NO and Cu^{+} species over Cu/SSZ-13 and Cu/SAPO-34 zeolites: the infrared absorption peak at 1805–1820 cm^{-1} and 1660–1720 cm^{-1} could be assigned to mono-nitroso Cu^{+}–NO complex and di-nitroso Cu^{+}–$(NO)_2$ complex, respectively. In addition, NO could also coordinate with hydrated Cu^{2+} species ($[Cu(OH)^{+}]$) to form the IR band at around 1790 cm^{-1}, which was confirmed by a newly formed hydroxyl vibrational absorption peak at 3668 cm^{-1}. Moreover, NO could also interact with dimeric Cu^{2+} species ($[Cu–O–Cu]^{2+}$) to form two kinds of IR absorption bands at 1712 cm^{-1} and 1887 cm^{-1}, which were attributed to the adsorption of NO on the Cu^{II}–O bridge bonds, and the direct adsorption of NO on Cu^{II} in $[Cu–O–Cu]^{2+}$ dimers, respectively. Giordanino *et al.*[131] summarized the FTIR bands after CO adsorption or NO adsorption over different Cu-based zeolites and revealed that the preparation method of catalysts and testing conditions (temperature, NO pressure, oxidation or reduction atmosphere) of FTIR experiments could resulted in slightly shift of FTIR bands for Cu–NO or Cu–CO complexes over different Cu-based zeolites. Base on above literature, the typical assignments of FTIR bands after CO adsorption or NO adsorption over different Cu-based zeolites are summarized in Tables 5 and 6, respectively.

Infrared spectroscopy of NO or CO adsorption is a highly valuable tool to provide information about the chemical nature of metal species in zeolites, such as the oxidation state, coordination environment, which are important in NH_3-SCR

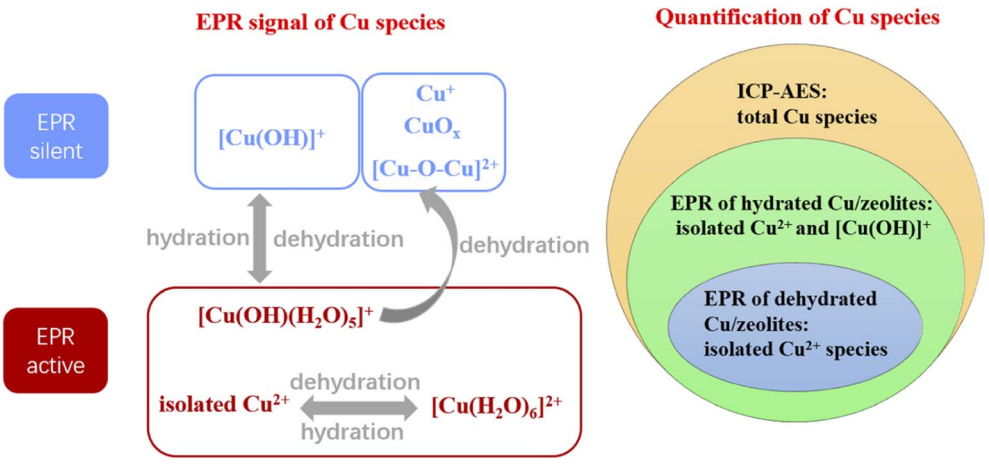

Fig. 4 Summary on the EPR determination and quantification of Cu species in Cu/zeolite.

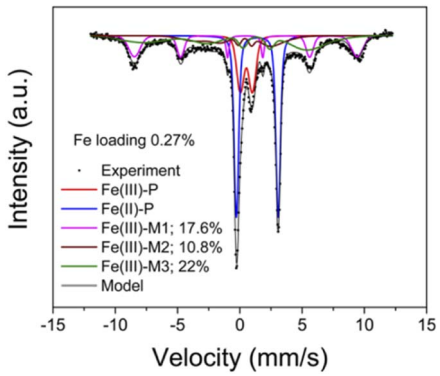

Fig. 5 Mössbauer spectroscopy of the ambient ^{57}Fe/SSZ-13 sample measured at 8 K. Peak fitting results and percentages of different components, Fe(III)-P, Fe(II)-P, Fe(III)-M are also displayed[144] (with permission from ACS publications).

reactions.[115,138,139] Through *in situ* adsorption of CO and NO infrared experiments, researchers had detailly investigated the distribution of Cu species on Cu/SSZ-13 zeolites under different pretreatment conditions, which provided valuable information for the understanding of detailed NH_3-SCR reaction mechanism.[7,14,127,129] However, the quantitative of various metal species by IR bands are difficult, as the unknown extinction coefficients of different adsorption band for metal species. In addition, the assignments of IR bands for NO or CO adsorption over different zeolites should be careful, as the interactions between zeolites with different framework and metal species were different, which would cause the shift of IR bands.[115] Moreover, the overlap of absorption peaks may occur at high adsorption pressure of CO or NO or when high loading of metal species was achieved at zeolites, which would make the assignment of IR bands difficult.[1,79] Therefore, care must be taken when general conclusions are drawn about the adsorption and reactive properties of metal species based on infrared spectroscopy of NO or CO adsorption in zeolites, which may should be supported by other characterization methods.

2.6 EPR

Electron paramagnetic resonance (EPR) is a magnetic resonance technology based on the magnetic moment of unpaired electrons which move around the nucleus and spin at the same time, resulting in electric current and magnetic moment.[140] Under an external electromagnetic field, the electrons with low energy levels can be excited to high energy levels by absorbing microwave energy, resulting in electron paramagnetic resonance. The *g* factor (spectral splitting factor) in paramagnetic resonance spectra which reflecting the local magnetic field information can be used to analyze the chemical environments of metal atoms.[21,43]

EPR spectroscopy has been successfully used to characterize the coordination environment and local structure of copper species in Cu-based zeolites.[22] As Cu^+ lacks paramagnetic electrons, $[Cu(OH)]^+$ has the pseudo Jahn–Teller effect, CuO_x clusters and $[Cu–O–Cu]^{2+}$ have antiferromagnetic interactions, these copper species are EPR silent species.[27] However, under hydration, $[Cu(OH)]^+$ species can be converted into $[Cu(OH)(H_2O)_5]^+$ species with EPR activity and thus be detected by EPR. In contrast, when dehydrated, $[Cu(OH)(H_2O)_5]^+$ species can be transformed into $[Cu(OH)]^+$ species, or be automatically reduced to Cu^+ species or be condensed to form $[Cu–O–Cu]^{2+}$ or CuO_x species, which are all EPR silent species. On the other hand, isolated Cu^{2+} species, either in the hydrated form ($[Cu(H_2O)_6]^{2+}$ or $[Cu(OH)(H_2O)_5]^+$) or dehydrated form (Cu^{2+}), are paramagnetic and can be detected by EPR.[27,77] Therefore, the relative content of $[Cu(OH)]^+$ and isolated Cu^{2+} species on Cu-based zeolites can be quantitatively calculated by EPR spectroscopy through determining the Cu-based zeolites under dehydration and hydration conditions, as described in Fig. 4.

Gao *et al.*[27] had quantitatively determining the content of various Cu species on Cu/SSZ-13 zeolites by combing EPR experiments under hydrated and dehydrated conditions with ICP-AES method. As summarized in Fig. 5, firstly, the content of isolated Cu^{2+} species can be calculated by EPR spectra of dehydrated Cu/SSZ-13 zeolites. Secondly, the total content of

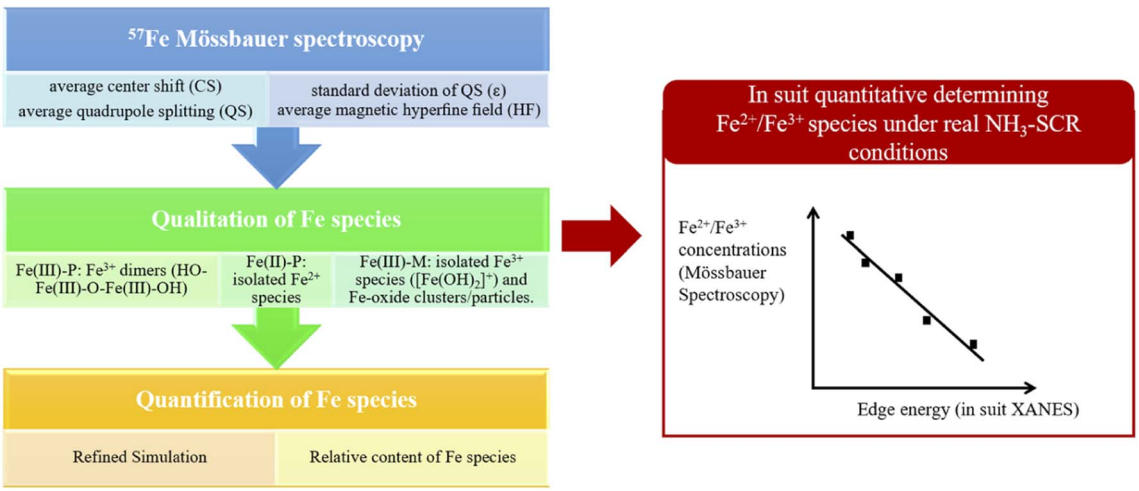

Fig. 6 Summary on the determination of Fe species in Fe/zeolite by Mössbauer spectroscopy.

Table 7 Comparison on the experimental and computational results for NO frequencies in different Cu–NO complexes in FTIR spectra[124] (with permissions from ACS publications)

NO frequency (cm^{-1})	Experimental results	Computational results
Cu^{2+}–NO	1850–1950	1895–1932
$[Cu(II)OH]^{+}$–NO	1870–1915	1874, 1907
Cu^{+}–NO	1770–1808	1794, 1788, 1795
Cu–N_2O	~2250	2367, 2339, 2362
Cu^{+}–NO^{+}	2160–2170	—

isolated Cu^{2+} species and $[Cu(OH)]^{+}$ species can be measured by EPR spectra of hydrated Cu/SSZ-13 zeolites; then the content of $[Cu(OH)]^{+}$ species on Cu/SSZ-13 zeolites can be calculated by the difference between the above two EPR spectra. Thirdly, the total content of all the Cu species on Cu/SSZ-13 zeolites can be measured by ICP-AES analysis. Therefore, the total content of copper species without EPR activity (such as Cu^{+}, $[Cu–O–Cu]^{2+}$ and CuO_x) can be calculated by combining the quantitative results of ICP-ASE and EPR experiments. Based on the quantitative determining of various Cu species on Cu/SSZ-13 zeolites, Gao *et al.*[27] found that the isolated Cu^{2+} species showed good hydrothermal stability in NH_3-SCR. In contrast, during the hydrothermal aging process, the $[Cu(OH)]^{+}$ species in Cu/SSZ-13 zeolites would gradually transform into CuO_x species, which had almost no NH_3-SCR activity but high activity to the side reactions of ammonia oxidation, and eventually cause the decrease of NH_3-SCR activity.

EPR spectra can also be used to distinguish the location and distance of isolated Cu^{2+} species. Gao *et al.*[78] had estimated the Cu–Cu distance of isolated Cu^{2+} ions in Cu/SSZ-13 zeolite based on the line broadening of EPR spectra. They found that the Cu–Cu distance was greater than 20 Å at low copper loadings, indicating that there was allowed only one Cu^{2+} ions within one hexagonal unit cell. As the Cu loading increased, the Cu–Cu distance decreased significantly, indicating that several Cu^{2+} ions were located in the large CHA cages and were close to the eight-membered rings.

In Fe-based zeolites, EPR spectra can be used to selectively detect Fe^{3+} species, as Fe^{2+} was silent in EPR spectra due to the lack of paramagnetic electrons. According to literature,[73,141,142] the EPR signal at $g = 4.3$ can be attributed to the tetrahedral Fe^{3+} species in the framework of zeolites, while the signa at $g =$ 6.0 and 8.8 are attributed to the distorted tetrahedral Fe^{3+} species and octahedral coordinated Fe^{3+} species, respectively. In addition, the highly symmetric octahedral coordinated Fe^{3+}, which are the predominant active species in NH_3-SCR, has characteristic EPR signals at $g = 2.0$; while the aggregated Fe_xO_y species show EPR characteristic signals at $g = 2.3$. Li *et al.*[73] had prepared Fe-ZSM-5 zeolites with different iron content by one-pot method, and found that the NH_3-SCR catalytic activity of Fe-ZSM-5 were positively correlated with the EPR iron species at $g = 2.0$ in the EPR spectra, which supported the above assignments. However, Shen *et al.*[141] had investigated the distribution of Fe^{3+} species in Fe/Beta zeolites by UV-vis and *in situ* EPR spectra and found that the isolated Fe^{3+} species in distorted tetrahedral ($g = 6$) and octahedral ($g = 8.8$) environments showed higher NH_3-SCR activity, while those in tetrahedral framework environments ($g = 4.3$) exhibited lower activity. The controversial results of EPR spectra over different Fe-based zeolites demonstrates that the differences in zeolite support, in the type and content of iron species and in the different experimental conditions could bring in discrepancies in the EPR spectra, which should be carefully analyzed considering the detailed experimental conditions of EPR spectra or by combining with other characterizations such as UV-vis, FTIR or XAFS.[13]

EPR is a powerful tool for determining metal species in zeolites with high sensitivity, which can provide qualitative and

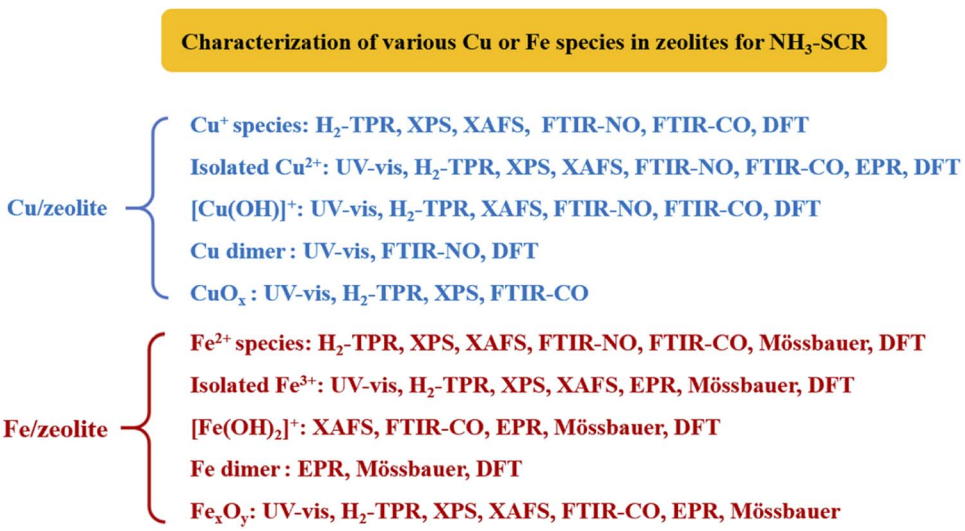

Fig. 7 The characterization methods of various Cu or Fe species in zeolites for NH_3-SCR.

quantitative information on the oxidation state and chemical environment of paramagnetic metal ions by combining with other characterization methods such as ICP and UV-vis.[29] However, there are still some limitations in the application of EPR spectra. Firstly, the EPR spectra with high resolution can only be obtained under ultra-low temperature of about 155 K for Cu-based zeolites[78] and about 7 K for Fe-based zeolites,[24] in order to avoid the signal broadening due to the migration of metal species and the anti-ferromagnetic interactions. Secondly, EPR spectra of metal-based zeolites are highly sensitive to water and paramagnetic species, so the testing conditions of EPR spectra should be strictly controlled.[21] Thirdly, when the structure of zeolite support changes, the *g* value of EPR signal for the same kind of metal species may shift due to different interactions between metal species and zeolites, which made the assignment of EPR signal difficult.[109] Therefore, the EPR spectra should be analyzed carefully according to the preparation method, zeolite support and metal content of catalysts, or by combining with other characterizations.

2.7 Mössbauer spectroscopy

Mössbauer spectroscopy is a kind of gamma ray spectrum based on "Mössbauer effect", *i.e.*, "the emission and subsequent resonant absorption of nuclear gamma rays by the nuclei of certain atoms embedded in a solid material".[143] When the energy of the gamma ray equal to the energy of nuclear energy level transition, the resonant absorption phenomenon can be observed in Mössbauer spectroscopy. Mössbauer spectroscopy can be used to study the chemical valence or oxidation state, magnetic properties, coordination numbers and electron density of specific atoms. However, though the "Mössbauer effect" of more than 80 isotopes is measurable, only two of them (^{57}Fe, ^{119}Sn) are applied in practice due to the restrict testing conditions and equipment.[143] As the obtaining of Mössbauer spectrum require the gamma ray source with high energy at low temperature, the further application of Mössbauer spectrum is greatly limited.

^{57}Fe Mössbauer spectroscopy conducting at cryogenic temperatures (8 K) can prevent signal loss caused by recoil of mobile species, and are proved to be more accurate than UV-vis and H_2-TPR in quantification of Fe species in zeolites.[68] According to previous studies,[13,23,24,68] four key parameters, *i.e.* average center shift (CS, mm s^{-1}), average quadrupole splitting (QS, mm s^{-1}), standard deviation of QS (ε, mm s^{-1}) and average magnetic hyperfine field (HF, Tesla) could be used to distinguish different Fe species in the Mössbauer spectroscopy of Fe/SSZ-13 zeolites.[57] Generally, the component with a CS value of $\sim$1.4 mm s^{-1} is attributed to Fe(II) species, while those with CS value of $\sim$0.5 mm s^{-1} can be assigned to Fe(III) species. Also, the paramagnetic Fe species give doublet features in Mössbauer spectroscopy (designated as P), while the magnetic Fe species display sextet signals (designated as M).[13,23,24,68] Based on above features, the Fe species in Fe/SSZ-13 zeolites can be distinguished and divided into three types:[13] Fe(III)-P representing Fe^{3+} dimers (HO–Fe(III)–O–Fe(III)–OH), Fe(II)-P assigning to isolated Fe^{2+} species, and Fe(III)-M to a mixture of isolated Fe^{3+} species ($[Fe(OH)_2]^+$) and Fe-oxide clusters/particles. By spectra deconvolution, the relative percentages of three types of Fe species in Fa/SSZ-13 zeolites can be estimated, as shown in Fig. 5, according to Gao and co-workers.[13]

Based on the quantification of ^{57}Fe Mössbauer spectroscopy and kinetic experiments, Gao and co-workers[13] had detailly investigated the active Fe sites in NH_3-SCR reactions over a series of Fe/SSZ-13 zeolites with differentiate iron contents. They found that the isolated Fe^{3+} species were the main active sites for standard NH_3-SCR at low temperatures ($\leq$260 °C), while the $[HO–Fe–O–Fe–OH]^{2+}$ species dominated the NH_3-SCR reactions in the high temperature range (260–550 °C). Moreover, the migration and aggregation of Fe species in Fe/SSZ-13 zeolites during the hydrothermal aging treatments had also been clearly clarified by ^{57}Fe Mössbauer spectroscopy:[24] the isolated Fe^{3+} species would gradually transform to $[HO–Fe–O–Fe–OH]^{2+}$ under mild hydrothermal conditions (600–700 °C), which was beneficial for the enhancement of NH_3-SCR activity. However, once the hydrothermal aging temperature exceeding 800 °C, the NH_3-SCR activity of aged Fe/SSZ-13 zeolites dramatically decreased due to serious framework dealumination, accompanying by the agglomeration of active isolated Fe^{3+} species to Fe_xO_y clusters or nanoparticles (without or with very low NH_3-SCR activity) and even the incorporation of Al into Fe_xO_y species (almost no SCR activity).

As the intensity of the Mössbauer signal is strongly temperature dependent (usually, the ultra-low testing temperature of 8 K is required for high resolution), the quantitative determination of the oxidation of Fe species in zeolites by *in situ* Mössbauer spectroscopy is not possible under real NH_3-SCR reactions at elevated temperatures.[145] However, Maier *et al.*[107] has developed an effective method to quantitative determining the oxidation state of Fe species in Fe/Bata zeolites under real NH_3-SCR conditions by combining *in situ* XANES and Mössbauer spectroscopy. They had obtained a linear correlation between the edge energy of the XANES and the oxidation state determined by Mössbauer spectroscopy, which in turn allowed them to determining the relative concentrations of Fe^{3+} and Fe^{2+} species under real NH_3-SCR conditions through *in situ* XANES with the aid of Mössbauer spectroscopy. In conclusion, the application and determination of Fe species in zeolites for NH_3-SCR are summarized in Fig. 6.

Compared with UV-vis, H_2-TPR and EPR experiments, Mössbauer spectroscopy is the most accurate method for the simultaneously determination of both Fe^{2+} and Fe^{3+} species in zeolites with high resolution and sensitivity.[13,24] In addition, only several type of nucleuses (^{57}Fe and ^{119}Sn) have the resonance absorption of Mössbauer effect, the determination of Mössbauer spectroscopy is not disturbed by other elements, which guarantees the high accuracy of Mössbauer spectroscopy but also limits its application. Moreover, the high cost of equipment with γ-ray sources and the low testing temperature (8 K) for high resolution also limit its application.[143]

Table 8 The summarized applications and limitations of different characterization methods on the detecting of Fe and Cu species in zeolites for NH_3-SCR

Characterization methods	Fe species	Cu species	Limitation
UV-vis	(1) 200–300 nm: 220–250 nm belongs to the four-coordinated isolated Fe^{3+} species, 250–300 nm are related to isolated Fe^{3+} species with higher coordination number	(1) 210 and 280 nm: isolated Cu^{2+} species (charge transfer from lattice O^{2-} to Cu^{2+})	(1) Only Fe^{3+} and Cu^{2+} species can be detected, Fe^{2+} and Cu^{+} species are invisible in 200–800 nm of UV-vis spectra[62–64,66]
	(2) 300–400 nm: charge transition peak of octahedral coordination aggregated Fe^{3+} species such as small Fe_xO_y species	(2) *ca.* 750 nm: isolated Cu^{2+} species (d–d transitions of Cu^{2+} species with distorted octahedral coordination)[61–64]	(2) Only a semiquantitative method due to the unknown extinction coefficients of different adsorption band of various metal species[59,66]
	(3) >400 nm: Fe_2O_3 nanoparticles[34,59,60]	(3) 250 nm and 450 nm: CuO_x species (the charge transfer (250 nm) and d–d transition (450 nm) of octahedral coordinated Cu^{2+} in CuO_x species[25,61,62,65]	(3) Only the coordination state of metal species can be obtained, the detailed chemical structure of metal species cannot be determined[64,67]
H_2-TPR	(1) 380–430 °C: the reduction of isolated Fe^{3+} to Fe^{2+} species[24,69,70]	(1) 400 °C: the reduction of Cu^{2+}–2Z to Cu^{+} species	(1) Unable to determine irreducible metal species such as Cu^0 and Fe^0 in zeolites
	(2) 500–560 °C: the reduction of aggregated Fe_xO_y species[24,69,70]	(2) The reduction of $[Cu(OH)]^{+}$–Z to Cu^{+} at 250 °C, then Cu^{+} to Cu^0 at 360 °C (ref. 27, 74 and 77)	(2) The distinguish of reduction peak for various metal species are difficult as they may shift and overlap with each other[35]
	(3) 680–750 °C: the reduction of Fe_2O_3 nanoparticles[69]	(3) 300 °C: the reduction of CuO to Cu^0 species[27,29,74]	(3) The assignment of reduction peak should consider the zeolite support, metal content, preparation method of catalysts[62,75,78,80]
	(4) 900–1000 °C: the reduction of Fe^{2+} species in ion-exchange sites and high aggregated Fe_2O_3 or Fe_3O_4 particles[34,69,71–73]	(4) 700–900 °C: Cu^{+} at the ion-exchange site of zeolite be reduced to Cu^0 species[27,29]	(4) The automatic reduction of metal species in the dehydration pre-treatment process caused by adsorbed H_2O in zeolites may decrease the H_2 consumption[77,81]
			(5) The shape and area of reduction peak in the H_2-TPR experiments could be affected by the heating rate of temperature-programmed process[82]
XPS	(1) Fe^{2+} $2p_{3/2}$ and $2p_{1/2}$ signals are those located at binding energy of *ca.* 710 eV and 723 eV with satellite peaks at *ca.* 715 eV and 729 eV, respectively[74,84,92–94]	(1) Cu $2p_{1/2}$ peak splits into two signals at 952.3 ± 0.2 eV for Cu^{+} and at 953.6 ± 0.2 eV for Cu^{2+} species[84,85]	(1) Only elements with nano-scale thickness on the surface of zeolites can be detected[84,97,98]
	(2) Fe^{3+} $2p_{3/2}$ and $2p_{1/2}$ signals are those located at about 711 eV and 724 eV with satellite peaks at *ca.* 719 eV and 733 eV, respectively[92,96]	(2) The assignment of Cu $2p_{3/2}$ signals are controversial. Some researchers attributed the Cu $2p_{3/2}$ signals at 932.5 ± 0.2 eV for Cu^{+} and those at 933.7 ± 0.2 eV for Cu^{2+} species,[84–86] while others attributing them to CuO species and isolated Cu^{2+} species, respectively[87]	(2) The automatic reduction of Cu^{2+} or Fe^{3+} species under pretreatment conditions of ultra-high vacuum[99]
			(3) The assignment of XPS peak are sometimes difficult due to shift and overlapping of binding energy signals for metal species,[89,96] better be carefully taken and with the aid of ICP-AES, EPR, Auger electron spectra and UV-vis spectra[88–92,94,95]
XAFS	(1) Distinguish and quantification of Fe^{2+} and Fe^{3+} species in Fe/zeolites[107]	(1) Distinguish and quantification of Cu^{+} and Cu^{2+} species in Cu/zeolites[28,105]	(1) The signals of all absorbing atoms of one type in the sample may overlap at the edge, which made it difficult to distinguish different kind of species[102]
	(2) Obtain the local structure of Fe species such as coordination number and bond lengths for Fe–O and Fe–Fe coordination spheres[108]	(2) Obtain the local structure of Cu species such as coordination number and bond lengths for Cu–O and Cu–Cu coordination spheres[25,26]	(2) The accessibility of synchrotrons of X-ray is not easy, as beam times are scarce and need to be scheduled months ahead[104]

Table 8 (*Contd.*)

Characterization methods	Fe species	Cu species	Limitation
	(3) *Operando* XAS can be used to monitor the oxidation and reduction half-cycle of Fe species in real NH_3-SCR reaction conditions[109]	(3) *Operando* XAS can be used to monitor the oxidation and reduction half-cycle of Cu species under real NH_3-SCR reaction conditions[28,32,105,106]	
FTIR spectroscopy	(1) FTIR of adsorption CO: selectively detecting Fe^{2+} species by weak adsorption to form Fe^{2+}–CO species, while Fe^{3+}–OH could coordinated with CO to form Fe^{3+}–OH···CO species[58,122,126]	(1) FTIR of adsorption CO: selectively detecting Cu^{+} species by forming Cu^{+}–CO, Cu^{+}–$(CO)_2$ species; Cu^{2+}–CO can only be formed under excessive CO condition[127–129]	(1) The automatic reduction of Cu^{2+} or Fe^{3+} species under pretreatment conditions of ultra-high vacuum[115,123,124]
	(2) FTIR of adsorption NO: selectively detecting Fe^{2+} species by strong adsorption to form Fe^{2+}–NO, Fe^{2+}–$(NO)_2$ and Fe^{2+}–$(NO)_3$ species[24,125]	(2) FTIR of adsorption NO: both Cu^{+} and Cu^{2+} species can be detected by strong adsorption to form Cu^{2+}–NO, Cu^{+}–NO, Cu^{+}–$(NO)_2$ complexes; $[Cu(OH)]^{+}$ and $[Cu–O–Cu]^{2+}$ can also coordinated with NO to form IR signal[127,129,130]	(2) The assignment of IR bands should be careful due to shifting and overlapping of signals for metal species when catalysts with high metal content or complex composition[1,7,14,79,115,127,129]
			(3) Only a semiquantitative method due to the unknown extinction coefficients of different adsorption band of various metal species[148]
EPR	(1) EPR silent: Fe^{2+} species[13]	(1) EPR silent: Cu^{+}, $[Cu(OH)]^{+}$, CuO_x and $[Cu–O–Cu]^{2+}$ species[27]	(1) Low testing temperature (155 K for Cu-based zeolites and 7 K for Fe-based zeolites) is required for taking high-resolution EPR spectra so as to relieve the peak broadening resulting from metal mobility and antiferromagnetic interactions[24,78]
	(2) EPR active: Fe^{3+} species, including framework, extra-framework Fe^{3+} in zeolites and Fe^{3+} in Fe_xO_y clusters[73,141,142]	(2) EPR active: isolated Cu^{2+}, $[Cu(H_2O)_6]^{2+}$ and $[Cu(OH)(H_2O)_5]^{+}$ species[27,77]	(2) High sensitivity of EPR signal to H_2O and paramagnetic species[21]
		(3) The quantitative measuring of different Cu species in Cu/SSZ-13 can be achieved by combining EPR and ICP-AES method[27]	(3) The deviation of g values for metal species with different zeolite supports made the assignments of EPR signal difficult[109]
		(4) The Cu–Cu distance of isolated Cu^{2+} ions in Cu/SSZ-13 can be estimated by the line broadening of EPR spectra[78]	
Mössbauer spectroscopy	(1) Determination of Fe^{2+} and Fe^{3+} at the same time	Unavailable	(1) Only applicable to several nucleus with Mossbauer effect, such as ^{57}Fe and ^{119}Sn[143]
	(2) Distinguishing of different types of Fe species: Fe(III)-P representing Fe^{3+} dimers (HO–Fe(III)–O–Fe(III)–OH)), Fe(II)-P assigning to isolated Fe^{2+} species, and Fe(III)-M to a mixture of isolated Fe^{3+} species ($[Fe(OH)_2]^{+}$) and Fe-oxide clusters/particles[13,23,24,68]		(2) Super-low testing temperature (8 K) for high resolution[13,24,68]
			(3) High cost of equipment with γ-ray sources which are not easy to be available[143]
DFT	(1) Verify the spectral results of gas molecules adsorption (CO, NO, *etc.*)[124,127]		(1) Calculation results may deviate from the actual structures due to the saturation of the boundary of the cluster model with hydrogen atoms[56]
	(2) Determining the location and distribution of active sites on the catalysts[146,147]		(2) Zeolite with complex spatial structures would result in huge calculations and the loss of accuracy of calculation results sometimes[56]

Table 8 (*Contd.*)

Characterization methods	Fe species	Cu species	Limitation
	(3) Calculating the activation energy of the elementary reaction to reveal the rate-determining step for NH_3-SCR[146,147]		(3) Calculation results of some special systems were heavily dependent on the selection of calculation methods[56]
	(4) Determining the reaction pathway by calculating the intermediates species and transition state energy of NH_3-SCR reactions, *etc.*[28,32,56]		

2.8 DFT calculation

The density functional theory (DFT) calculation is another powerful tool to study the chemical state of metal species, the key reaction intermediates and the reaction mechanism of NH_3-SCR, which could be used to study the interactions between atoms or molecules with the catalysts from atomic-scale.

As a gas–solid multiphase reaction, the gas molecules adsorption process is important for the study of NH_3-SCR mechanism, which is usually investigated by experimental method such as FTIR spectra, XAFS, and reaction kinetics. DFT can be used to predict and verify the spectral results of gas molecules adsorption (CO, NO, N_2, NH_3, *etc.*) so as to investigate the key metal species and reaction mechanism of NH_3-SCR. Zhang *et al.*[124] had investigated the NO adsorption process over Cu-SSZ-13 zeolite by FTIR spectra and DFT calculations and found a perfect agreement between FTIR bands and DFT calculation results for the NO vibration frequencies, as shown in Table 7. Base on FTIR results and DFT calculations, they concluded that NO molecules did bind stronger on $[Cu(OH)]^+$ located in 8MR than isolated Cu^{2+} species in the 6MR of CHA structure in Cu/SSZ-13 zeolites, which indicated that Cu^{2+} ions were stabilized with ligands in 8MR of CHA cages in NH_3-SCR. Similarly, Corma *et al.*[127] had also clearly identified different kinds of Cu–NO complexes in Cu/SAPO-34 and Cu/SSZ-13 zeolites by combining FTIR spectra of NO adsorption and DFT calculations, which could be used to indirectly determining the distribution of Cu species in zeolites.

DFT can also be used to determine the distribution and spatial location of metal active sites, the key intermediate species and to reaction pathway in NH_3-SCR. Li *et al.*[146] had explored the possible locations of Cu^{2+} species in Cu/SAPO-18 by DFT calculations and EPR experiments. They calculated and found two of seven possible locations of Cu^{2+} species were the most stable energy state, and then revealed the NH_3-SCR reaction mechanism over Cu/SAPO-18 based on that. Mao *et al.*[147] calculated the binding energy of Cu^{2+} species on five type of ion exchange sites in SAPO-34 and found that Cu^{2+} species located in the 6MR plane with slightly off-center position had the lowest binding energy, which were the most stable exchange sites for Cu^{2+} in SAPO-34. Further research indicated that those stable Cu^{2+} species were the main active sites for Cu/SAPO-34 zeolites in NH_3-SCR.

McEwen *et al.*[28] investigated the oxidation state and coordination environment of Cu species in Cu/SSZ-13 under standard SCR or rapid SCR conditions by *operando* XAS with the aid of DFT calculations. They found that the oxidation state of Cu species changed with reaction conditions: four-fold-coordinated Cu^{2+} species dominated the Cu/SSZ-13 zeolites under fast and slow SCR conditions, in which the NO_2/NO_x ratios were 0.5 and 1 in the feed gas, respectively. In contrast, mixed Cu^+ and Cu^{2+} oxidation states were observed under standard SCR conditions without NO_2 in the feed gas, which indicated a reduction in the average Cu coordination and highlighted the role of Cu redox chemistry in NH_3-SCR process. Based on DFT calculation and kinetic experiments, Gao *et al.*[32] studied the oxidation half-cycle of Cu^+ to Cu^{2+} process over Cu/SSZ-13 in NH_3-SCR and found that the isolated Cu^+ species were unable to complete oxidation half-cycle at low temperatures, which process could only occur with the participation of two isolated Cu^+ ions by forming $[Cu^I(NH_3)_2]^+$–O_2–$[Cu^I(NH_3)_2]^+$ intermediates. In addition, the above oxidation half-cycle was the rate-determining step for NH_3-SCR at low temperatures, which was confirmed by DFT calculations.

Recently, Guan *et al.*[56] reviewed the application of DFT in NH_3-SCR research from the aspects of surface adsorption, metal active sites characteristics, reaction mechanism, hydrothermal aging mechanism and poisoning mechanism in catalysts. DFT calculations can obtain a lot of information of catalysts in NH_3-SCR, which can not only verify the experimental characterization results to make them more reliable, but also reveal the underlying causes of experimental results from microscopic atomic level. The current use of DFT in NH_3-SCR included: determining the location and distribution of active sites on the catalysts, calculating the activation energy of the elementary reaction to reveal the rate-determining step for NH_3-SCR, determining the reaction pathway by calculating the intermediates species and transition state energy of NH_3-SCR reactions, *etc.*

Though DFT is a universal method to investigate the physicochemical and reactivity properties of catalysts which is not restricted by the research project or the research process, there are still shortcomings. Firstly, when constructing models, saturation of the boundary of the cluster model with hydrogen atoms may cause deviations from the actual structures. Secondly, zeolite with complex spatial structures would result in huge calculations and the loss of accuracy of calculation results sometimes. Thirdly, the DFT calculation results of some special systems were heavily dependent on the selection of calculation methods. However, the development of calculation software and methods may help to solve those problem. By combining

with advanced experimental methods, DFT calculation has become one of the most important tool to investigate the reaction mechanism of NH_3-SCR.

3 Conclusions and outlook

Cu-based and Fe-based zeolites are promising catalysts for NH_3-SCR due to the high catalytic activity, wide temperature window and good hydrothermal stability. The detailed investigation of NH_3-SCR mechanism based on Cu-based and Fe-based zeolites are important for further development of high-efficiency NH_3-SCR catalysts, which should be based on the accurate determining of active metal sites. Fig. 7 summarizing the effective characterization methods of various Cu or Fe species in zeolites for NH_3-SCR. As also summarized in Table 8, UV-vis, H_2-TPR, XPS, XAFS, FTIR (adsorption of CO or NO), EPR, Mössbauer spectroscopy and DFT calculations introduced in this review are characteristic methods to determine the type, content, distribution or even local structure of various Cu or Fe species in zeolites, though they have different applicability and limitations. In addition, the accurate qualitative and quantitative determination of various metal active sites in Cu-based or Fe-based zeolites usually requires a combination of several characterization methods by considering the preparation method of catalysts and by careful analyzing the characterization results. Moreover, off-line characterization methods often cannot precisely reveal the chemical environment of metal active species in real NH_3-SCR conditions, as well as the interactions between active sites with reactants. Therefore, the *in situ* or *operando* characterization methods such as *in situ* IR, *in situ* UV-vis, *in situ* EPR, *operando* XAFS, *etc.*, as well as DFT calculations should also be applied to more accurately reveal the activation and reaction process of active species on the catalysts so as to reveal the detailed reaction mechanism of NH_3-SCR.

Author contributions

Jialing Chen: conception, investigation and writing-review & editing; Wei Huang: investigation and methodology; Sizhuo Bao: investigation and methodology; Wenbo Zhang: investigation and methodology; Tingyu Liang: methodology, and review & editing; Shenke Zheng: IR spectroscopy analysis; Lan Yi: UV-vis analysis; Li Guo: H_2-TPR analysis; Xiaoqin Wu: review & editing. All authors have read and agreed to the published version of the manuscript.

Conflicts of interest

There are no conflicts to declare.

Acknowledgements

This article is devoted to the 60th birthday of our beloved Prof. Jianguo Wang (Shanxi Institute of Coal Chemistry, University of Chinese Academy of Sciences). We are grateful for the financial supports of the National Natural Science Foundation of China (22002114 and 22102124), the National Innovation and Entrepreneurship Training Program for College Students (201810488016); the Education Department of Hubei Province (Q20211501), the Open Fund of Key Laboratory of Hubei Province for Coal Conversion and New Carbon Materials (WKDM202208). We would like to thank Mr Guohong Zhang, Jinhui Zhou and Feizhou Wang at the Analytical & Testing Center of Wuhan University of Science and Technology for the help on XPS and FTIR experimental method.

References

1 U. Deka, I. Lezcano-Gonzalez, B. M. Weckhuysen and A. M. Beale, *ACS Catal.*, 2013, **3**, 413–427.
2 L. Han, S. Cai, M. Gao, J.-y. Hasegawa, P. Wang, J. Zhang, L. Shi and D. Zhang, *Chem. Rev.*, 2019, **119**, 10916–10976.
3 L. Zhang, Q. Wu, X. Meng, U. Müller, M. Feyen, D. Dai, S. Maurer, R. McGuire, A. Moini, A.-N. Parvulescu, W. Zhang, C. Shi, T. Yokoi, X. Pan, X. Bao, H. Gies, B. Marler, D. E. De Vos, U. Kolb and F.-S. Xiao, *React. Chem. Eng.*, 2019, **4**, 975–985.
4 F. Liu, Y. Yu and H. He, *Chem. Commun.*, 2014, **45**, 8445–8463.
5 Y. Yue, B. Liu, P. Qin, N. Lv, T. Wang, X. Bi, H. Zhu, P. Yuan, Z. Bai, Q. Cui and X. Bao, *Chem. Eng. J.*, 2020, **398**, 125515–125527.
6 A. M. Beale, I. Lezcano-Gonzalez, T. Maunula and R. G. Palgrave, *Catal., Struct. React.*, 2015, **1**, 25–34.
7 T. Jiang and R. F. Lobo, in *Structure and Reactivity of Metals in Zeolite Materials*, ed. J. Pérez Pariente and M. Sánchez-Sánchez, Springer International Publishing, Cham, 2018, DOI: 10.1007/430_2018_23, pp. 155–178.
8 J. Wang, H. Zhao, G. Haller and Y. Li, *Appl. Catal., B*, 2017, **202**, 346–354.
9 C. Paolucci, J. R. Di Iorio, F. H. Ribeiro, R. Gounder and W. F. Schneider, in *Advances in Catalysis*, ed. C. Song, 2016, vol. 59, pp. 1–107.
10 R. Zhang, N. Liu, Z. Lei and B. Chen, *Chem. Rev.*, 2016, **116**, 3658–3721.
11 T. J. Toops, J. A. Pihl and W. P. Partridge, in *Urea-SCR Technology for deNOx After Treatment of Diesel Exhausts*, ed. I. Nova and E. Tronconi, Springer New York, New York, 2014, DOI: 10.1007/978-1-4899-8071-7_4, pp. 97–121.
12 F. Gao, E. D. Walter, M. Kollar, Y. Wang, J. Szanyi and C. H. F. Peden, *J. Catal.*, 2014, **319**, 1–14.
13 F. Gao, Y. Zheng, R. K. Kukkadapu, Y. L. Wang, E. D. Walter, B. Schwenzer, J. Szanyi and C. H. F. Peden, *ACS Catal.*, 2016, **6**, 2939–2954.
14 F. Gao, *ChemCatChem*, 2020, **10**, 1324.
15 Y. Shan, J. Du, Y. Zhang, W. Shan, X. Shi, Y. Yu, R. Zhang, X. Meng, F. S. Xiao and H. He, *Natl. Sci. Rev.*, 2021, **8**, 134–153.
16 A. M. Beale, F. Gao, I. Lezcano-Gonzalez, C. H. Peden and J. Szanyi, *Chem. Soc. Rev.*, 2015, **44**, 7371–7405.
17 A. Wang, Y. Chen, E. D. Walter, N. M. Washton, D. Mei, T. Varga, Y. Wang, J. Szanyi, Y. Wang, C. H. F. Peden and F. Gao, *Nat. Commun.*, 2019, **10**, 1137–1147.

18 W. Zhang, J. Chen, L. Guo, W. Zheng, G. Wang, S. Zheng and X. Wu, *J. Fuel Chem. Technol.*, 2021, **49**, 1294–1315.
19 W. Zheng, J. Chen, L. Guo, W. Zhang, H. Zhao and X. Wu, *J. Fuel Chem. Technol.*, 2020, **48**, 1193–1210.
20 Y. Zhang, J. Zhang, H. Wang, W. Yang, C. Wang, Y. Peng, J. Chen, J. Li and F. Gao, *J. Phys. Chem. C*, 2022, **126**, 8720–8733.
21 Y. Wu, Y. Ma, Y. Wang, K. G. Rappé, N. M. Washton, Y. Wang, E. D. Walter and F. Gao, *J. Am. Chem. Soc.*, 2022, **144**, 9734–9746.
22 Y. Zhang, Y. Peng, J. Li, K. Groden, J.-S. McEwen, E. D. Walter, Y. Chen, Y. Wang and F. Gao, *ACS Catal.*, 2020, **10**, 9410–9419.
23 F. Gao, M. Kollár, R. K. Kukkadapu, N. M. Washton, Y. Wang, J. Szanyi and C. H. Peden, *Appl. Catal., B*, 2015, **164**, 407–419.
24 L. Kovarik, N. M. Washton, R. K. Kukkadapu, A. Devaraj, A. Wang, Y. Wang, J. Szanyi, C. H. F. Peden and F. Gao, *ACS Catal.*, 2017, **7**, 2458–2470.
25 S. T. Korhonen, D. W. Fickel, R. F. Lobo, B. M. Weckhuysen and A. M. Beale, *Chem. Commun.*, 2011, **47**, 800–802.
26 U. Deka, A. Juhin, E. A. Eilertsen, H. Emerich, M. A. Green, S. T. Korhonen, B. M. Weckhuysen and A. M. Beale, *J. Phys. Chem. C*, 2012, **116**, 4809–4818.
27 J. Song, Y. L. Wang, E. D. Walter, N. M. Washton, D. H. Mei, L. Kovarik, M. H. Engelhard, S. Prodinger, Y. Wang, C. H. F. Peden and F. Gao, *ACS Catal.*, 2017, **7**, 8214–8227.
28 J. S. McEwen, T. Anggara, W. F. Schneider, V. F. Kispersky, J. T. Miller, W. N. Delgass and F. H. Ribeiro, *Catal. Today*, 2012, **184**, 129–144.
29 J. Xue, X. Wang, G. Qi, J. Wang, M. Shen and W. Li, *J. Catal.*, 2013, **297**, 56–64.
30 C. Paolucci, A. A. Parekh, I. Khurana, J. R. Di Iorio, H. Li, J. D. A. Caballero, A. J. Shih, T. Anggara, W. N. Delgass, J. T. Miller, F. H. Ribeiro, R. Gounder and W. F. Schneider, *J. Am. Chem. Soc.*, 2016, **138**, 6028–6048.
31 B. Chen, R. Xu, R. Zhang and N. Liu, *Environ. Sci. Technol.*, 2014, **48**, 13909–13916.
32 F. Gao, D. Mei, Y. Wang, J. Szanyi and C. H. F. Peden, *J. Am. Chem. Soc.*, 2017, **139**, 4935–4942.
33 S. Zhao, L. Huang, B. Jiang, M. Cheng, J. Zhang and Y. Hu, *Chin. J. Catal.*, 2018, **39**, 800–809.
34 J. Chen, G. Peng, W. Zheng, W. Zhang, L. Guo and X. Wu, *Catal. Sci. Technol.*, 2020, **10**, 6583–6598.
35 J. Chen, G. Peng, T. Liang, W. Zhang, W. Zheng, H. Zhao, L. Guo and X. Wu, *Nanomaterials*, 2020, **10**, 2170.
36 S. Mohan, P. Dinesha and S. Kumar, *Chem. Eng. J.*, 2020, **384**, 123253–123262.
37 M. Jabłońska, *Mol. Catal.*, 2022, **518**, 112111.
38 H. Lei, V. Rizzotto, A. Guo, D. Ye, U. Simon and P. Chen, *Catalysts*, 2021, **11**, 52.
39 S. Zhang, L. Pang, Z. Chen, S. Ming, Y. Dong, Q. Liu, P. Liu, W. Cai and T. Li, *Appl. Catal., A*, 2020, **607**, 117855.
40 C. H. F. Peden, *J. Catal.*, 2019, **373**, 384–389.
41 Q. Liu, C. Bian, S. Ming, L. Guo, S. Zhang, L. Pang, P. Liu, Z. Chen and T. Li, *Appl. Catal., A*, 2020, **607**, 117865.
42 Y. Pu, X. Xie, W. Jiang, L. Yang, X. Jiang and L. Yao, *Chin. Chem. Lett.*, 2020, **31**, 2549–2555.
43 T. Andana, K. G. Rappé, F. Gao, J. Szanyi, X. Pereira-Hernandez and Y. Wang, *Appl. Catal., B*, 2021, **291**, 120054.
44 Z. Zhang, J. Li, J. Tian, Y. Zhong, Z. Zou, R. Dong, S. Gao, W. Xu and D. Tan, *Fuel Process. Technol.*, 2022, **230**, 107213.
45 J. Yang, Y. Huang, J. Su, L. Chen, M. Zhang, M. Gao, M. Yang, F. Wang, X. Zhang and B. Shen, *Sep. Purif. Technol.*, 2022, **297**, 121544.
46 R. T. Guo, B. Qin, L. G. Wei, T. Y. Yin, J. Zhou and W. G. Pan, *Phys. Chem. Chem. Phys.*, 2022, **24**, 363–6382.
47 N. Zhang, H. He, D. Wang and Y. Li, *J. Solid State Chem.*, 2020, **289**, 121464.
48 M. Cai, X. Bian, F. Xie, W. Wu and P. Cen, *Catalysts*, 2021, **11**, 361.
49 W. Shan, Y. Yu, Y. Zhang, G. He and H. He, *Catal. Today*, 2020, **376**, 292–301.
50 S. J. Park, *Catalysts*, 2021, **11**, 1519.
51 Z. Lian, Y. Li, W. Shan and H. He, *Catalysts*, 2020, **10**, 1421.
52 C. Liu, H. Wang, Z. Zhang and Q. Liu, *Catalysts*, 2020, **10**, 1034.
53 J. Xu, Y. Zhang, X. Zou, T. Tang, Q. Zhang, F. Guo and H. Liu, *New J. Chem.*, 2022, **46**, 2053–2067.
54 G. Xu, X. Guo, X. Cheng, J. Yu and B. Fang, *Nanoscale*, 2021, **13**, 7052–7080.
55 K. Guo, J. Ji, W. Song, J. Sun, C. Tang and L. Dong, *Appl. Catal., B*, 2021, **297**, 120388.
56 B. Guan, H. Jiang, Y. Wei, Z. Liu, X. Wu, H. Lin and Z. Huang, *Mol. Catal.*, 2021, **510**, 111704.
57 M. Li, Y. Guo and J. Yang, *ChemCatChem*, 2020, **19**, 5599–5610.
58 J. Kim, A. Jentys, S. M. Maier and J. A. Lercher, *J. Phys. Chem. C*, 2013, **117**, 986–993.
59 J. Pérez-Ramírez, J. Groen, A. Brückner, M. S. Kumar, U. Bentrup, M. Debbagh and L. Villaescusa, *J. Catal.*, 2005, **232**, 318–334.
60 R. Nedyalkova, S. Shwan, M. Skoglundh and L. Olsson, *Appl. Catal., B*, 2013, **138–139**, 373–380.
61 H. Praliaud, S. Mikhailenko, Z. Chajar and M. Primet, *Appl. Catal., B*, 1998, **16**, 359–374.
62 Z. Zhao, R. Yu, R. Zhao, C. Shi, H. Gies, F. S. Xiao, D. D. Vos, T. Yokoi, X. Bao and U. Kolb, *Appl. Catal., B*, 2017, **217**, 421–428.
63 A. El-Trass, H. ElShamy, I. El-Mehasseb and M. El-Kemary, *Appl. Surf. Sci.*, 2012, **258**, 2997–3001.
64 M. H. Groothaert, J. A. van Bokhoven, A. A. Battiston, B. M. Weckhuysen and R. A. Schoonheydt, *J. Am. Chem. Soc.*, 2003, **125**, 7629–7640.
65 I. Lezcano-Gonzalez, U. Deka, H. E. V. D. Bij, P. Paalanen, B. Arstad, B. M. Weckhuysen and A. M. Beale, *Appl. Catal., B*, 2014, **154–155**, 339–349.
66 J. Pérez-Ramírez, M. Santhosh Kumar and A. Brückner, *J. Catal.*, 2004, **223**, 13–27.
67 B. Ipek, M. J. Wulfers, H. Kim, F. Goltl, I. Hermans, J. P. Smith, K. S. Booksh, C. M. Brown and R. F. Lobo, *ACS Catal.*, 2017, **7**, 4291–4303.

68 A. Wang, Y. Wang, E. D. Walter, R. K. Kukkadapu, Y. Guo, G. Lu, R. S. Weber, Y. Wang, C. H. F. Peden and F. Gao, *J. Catal.*, 2018, **358**, 199–210.
69 S. Brandenberger, O. Kröcher, M. Casapu, A. Tissler and R. Althoff, *Appl. Catal., B*, 2011, **101**, 649–659.
70 K. Niu, G. Li, J. Liu and Y. Wei, *J. Solid State Chem.*, 2020, **287**, 121330–1213336.
71 X. Shi, H. He and L. Xie, *Chin. J. Catal.*, 2015, **36**, 649–656.
72 K. Krishna, G. B. F. Seijger, C. M. V. D. Bleek, M. Makkee and H. P. A. Calis, *Catal. Lett.*, 2003, **86**, 121–132.
73 E. Yuan, G. Wu, W. Dai, N. Guan and L. Li, *Catal. Sci. Technol.*, 2017, **7**, 3036–3044.
74 J. H. Kwak, H. Zhu, J. H. Lee, C. H. Peden and J. Szanyi, *Chem. Commun.*, 2012, **48**, 4758–4760.
75 H. Wang, R. Xu, Y. Jin and R. Zhang, *Catal. Today*, 2019, **327**, 295–307.
76 Y. Cui, Y. Wang, E. D. Walter, J. Szanyi, Y. Wang and F. Gao, *Catal. Today*, 2019, **339**, 233–240.
77 F. Gao, N. M. Washton, Y. Wang, M. Kollár, J. Szanyi and C. H. F. Peden, *J. Catal.*, 2015, **331**, 25–38.
78 F. Gao, E. D. Walter, E. M. Karp, J. Luo, R. G. Tonkyn, J. H. Kwak, J. Szanyi and C. H. F. Peden, *J. Catal.*, 2013, **300**, 20–29.
79 F. Lin, T. Andana, Y. Wu, J. Szanyi, Y. Wang and F. Gao, *J. Catal.*, 2021, **401**, 70–80.
80 J. Li, N. Wilken, K. Kamasamudram and N. W. Currier, *Top. Catal.*, 2013, **56**, 201–204.
81 F. Gao, J. H. Kwak, J. Szanyi and C. H. F. Peden, *Top. Catal.*, 2013, **56**, 1441–1459.
82 J. M. Kanervo and A. O. I. Krause, *J. Catal.*, 2002, **207**, 57–65.
83 J. H. Lee, Y. J. Kim, T. Ryu, P. S. Kim, H. K. Chang and S. B. Hong, *Appl. Catal., B*, 2017, **200**, 428–438.
84 Q. Ye, L. Wang and R. T. Yang, *Appl. Catal., A*, 2012, **427**, 24–34.
85 J. Chastain and R. C. King Jr, *Handbook of X-ray photoelectron spectroscopy*, J Perkin-Elmer Corporation, 1992.
86 L. Xu, C. Shi, B. B. Chen, Q. Zhao, Y. J. Zhu, H. Gies, F. S. Xiao, D. De Vos, T. Yokoi, X. H. Bao, U. Kolb, M. Feyen, S. Maurer, A. Moini, U. Muller and W. P. Zhang, *Microporous Mesoporous Mater.*, 2016, **236**, 211–217.
87 H. Jiang, B. Guan, H. Lin and Z. Huang, *Fuel*, 2019, **255**, 115587.
88 H. Yang, X. Cui, S. Li, Y. Cen, T. Deng, J. Wang, U. Olsbye and W. Fan, *Microporous Mesoporous Mater.*, 2020, **305**, 110381.
89 H. Yang, Y. Chen, X. Cui, G. Wang, Y. Cen, T. Deng, W. Yan, J. Gao, S. Zhu and U. Olsbye, *Angew. Chem., Int. Ed.*, 2018, **130**, 1854–1858.
90 J. Gong, H. Yue, Y. Zhao, S. Zhao, L. Zhao, J. Lv, S. Wang and X. Ma, *J. Am. Chem. Soc.*, 2012, **134**, 13922–13925.
91 S. Velu, K. Suzuki, M. Vijayaraj, S. Barman and C. S. Gopinath, *Appl. Catal., B*, 2005, **55**, 287–299.
92 F. Mercier, N. Thromat and C. Beaucaire, *Appl. Surf. Sci.*, 2000, **165**, 2880302.
93 J. Gurgul, K. Łątka, I. Hnat, J. Rynkowski and S. Dzwigaj, *Microporous Mesoporous Mater.*, 2013, **168**, 1–6.
94 T. Yamashita and P. Hayes, *Appl. Surf. Sci.*, 2008, **254**, 2441–2449.
95 D. D. Hawn and B. M. DeKoven, *Surf. Interface Anal.*, 1987, **10**, 63–74.
96 P. Boron, L. Chmielarz, J. Gurgul, K. Łatka, B. Gil, B. Marszałek and S. Dzwigaj, *Microporous Mesoporous Mater.*, 2015, **203**, 73–85.
97 Y. Li, X. Han, Y. Hou, Y. Guo, Y. Liu, N. Xiang, Y. Cui and Z. Huang, *Chin. J. Catal.*, 2017, **38**, 1831–1841.
98 Y. Yue, H. Liu, P. Yuan, C. Yu and X. Bao, *Sci. Rep.*, 2015, **5**, 9270–9279.
99 M. Milanesio, G. Croce, D. Viterbo, H. O. Pastore, A. J. dos Santos Mascarenhas, E. C. de Oliveira Munsignatti and L. Meda, *J. Phys. Chem. A*, 2008, **112**, 13745.
100 B. Pereda-Ayo, U. D. L. Torre, M. J. Illán-Gómez, A. Bueno-López and J. R. González-Velasco, *Appl. Catal., B*, 2014, **147**, 420–428.
101 A. Boubnov, H. W. Carvalho, D. E. Doronkin, T. Günter, E. Gallo, A. J. Atkins, C. R. Jacob and J.-D. Grunwaldt, *J. Am. Chem. Soc.*, 2014, **136**, 13006–13015.
102 A. Williams, *Rev. Sci. Instrum.*, 1983, **54**, 193–197.
103 H. Maeda, T. Fukunaga, K. Suzuki, K. Osamura, M. Hida, H. Terauchi and N. Kamijo, *Jpn. J. Appl. Phys.*, 1988, **27**, L938–L940.
104 P. Behrens, *Molecular Sieves – Science and Technology*, 2004, vol. 4, pp. 427–466.
105 K. A. Lomachenko, E. Borfecchia, C. Negri, G. Berlier, C. Lamberti, P. Beato, H. Falsig and S. Bordiga, *J. Am. Chem. Soc.*, 2016, **138**, 12025–12028.
106 K. Ueda, J. Ohyama and A. Satsuma, *Chem. Lett.*, 2017, **46**, 1390–1392.
107 S. M. Maier, A. Jentys, E. Metwalli, P. Müller-Buschbaum and J. A. Lercher, *J. Phys. Chem. Lett.*, 2011, **2**, 950–955.
108 D. E. Doronkin, M. Casapu, T. Günter, O. Müller, R. Frahm and J.-D. Grunwaldt, *J. Phys. Chem. C*, 2014, **118**, 10204–10212.
109 M. Hoj, M. J. Beier, J.-D. Grunwaldt and S. r. Dahl, *Appl. Catal., B*, 2009, **93**, 166–176.
110 Y. Xin, N. Zhang, X. Wang, Q. Li, X. Ma, Y. Qi, L. Zheng, J. A. Anderson and Z. Zhang, *Catal. Today*, 2019, **332**, 35–41.
111 K. A. Lomachenko, E. Borfecchia, C. Negri, G. Berlier, C. Lamberti, P. Beato, H. Falsig and S. Bordiga, *J. Am. Chem. Soc.*, 2016, **138**, 12025–12028.
112 F. Gao and J. Szanyi, *Nat. Catal.*, 2018, **1**, 174–175.
113 S. M. Maier, A. Jentys, M. Janousch and J. A. van Bekkum, *J. Phys. Chem. C*, 2012, **116**, 5846–5856.
114 I. A. Pankin, H. I. Hamoud, K. A. Lomachenko, S. B. Rasmussen, A. Martini, P. Bazin, V. Valtchev, M. Daturi, C. Lamberti and S. Bordiga, *Catal. Sci. Technol.*, 2021, **11**, 846–860.
115 Y. Zhang, Y. Peng, K. Li, S. Liu, J. Chen, J. Li, F. Gao and C. H. F. Peden, *ACS Catal.*, 2019, **9**, 6137–6145.
116 X. Wei, Q. Ke, H. Cheng, Y. Guo, Z. Yuan, S. Zhao, T. Sun and S. Wang, *Chem. Eng. J.*, 2019, **9**, 123491–123502.

117 R. P. Vélez, U. Bentrup, W. Grünert and A. Brückner, *Top. Catal.*, 2017, **60**, 1641–1652.
118 A. Martini, E. Borfecchia, K. A. Lomachenko, I. A. Pankin, C. Negri, G. Berlier, P. Beato, H. Falsig, S. Bordiga and C. Lamberti, *Chem. Sci.*, 2017, **8**, 6836–6851.
119 D. Sun, Q. Liu, Z. Liu, G. Gui and Z. Huang, *Catal. Today*, 2009, **132**, 122–126.
120 H. Zhu, J. H. Kwak, C. H. F. Peden and J. Szanyi, *Catal. Today*, 2013, **205**, 16–23.
121 P. R. Chen and U. Simon, *Catalysts*, 2016, **6**, 204.
122 I. Malpartida, E. Ivanova, M. Mihaylov, K. Hadjiivanov, V. Blasin-Aubé, O. Marie and M. Daturi, *Catal. Today*, 2010, **149**, 295–303.
123 H.-Y. Chen, M. Kollar, Z. Wei, F. Gao, Y. Wang, J. Szanyi and C. H. F. Peden, *Catal. Today*, 2019, **320**, 61–71.
124 R. Zhang, J.-S. McEwen, M. Kollár, F. Gao, Y. Wang, J. Szanyi and C. H. F. Peden, *ACS Catal.*, 2014, **4**, 4093–4105.
125 J. Szanyi, F. Gao, J. H. Kwak, M. Kollár, Y. Wang and C. H. F. Peden, *Phys. Chem. Chem. Phys.*, 2016, **18**, 10473–10485.
126 R. Kefirov, E. Ivanova, K. Hadjiivanov, S. Dzwigaj and M. Che, *Catal. Lett.*, 2008, **125**, 209–214.
127 P. Concepcion, M. Boronat, R. Millan, M. Moliner and A. Corma, *Top. Catal.*, 2017, **60**, 1653–1663.
128 A. Frache, M. Cadoni, C. Bisio, L. Marchese, A. J. S. Mascarenhas and H. O. Pastore, *Langmuir*, 2002, **18**, 6875–6880.
129 J. Szanyi, J. H. Kwak, H. Zhu and C. Peden, *Phys. Chem. Chem. Phys.*, 2013, **15**, 2368–2380.
130 M.-L. Tarot, E. E. Iojoiu, V. Lauga, D. Duprez, X. Courtois and F. Can, *Appl. Catal., B*, 2019, **250**, 355–368.
131 F. Giordanino, P. N. R. Vennestrm, L. F. Lundegaard, F. N. Stappen, S. Mossin, P. Beato, S. Bordiga and C. Lamberti, *Dalton Trans.*, 2013, **42**, 12741–12761.
132 C. Lamberti, S. Bordiga, M. Salvalaggio, G. Spoto, A. Zecchina, F. Geobaldo, G. Vlaic and M. Bellatreccia, *J. Phys. Chem. B*, 1997, **101**, 344–360.
133 C. Lamberti, S. Bordiga, A. Zecchina, M. Salvalaggio, F. Geobaldo and C. O. Areán, *J. Chem. Soc., Faraday Trans.*, 1998, **94**, 1519–1525.
134 G. Turnes Palomino, S. Bordiga, C. Lamberti, A. Zecchina and C. Otero Areán, in *Studies in Surface Science and Catalysis*, ed. R. Aiello, G. Giordano and F. Testa, Elsevier, 2002, vol. 142, pp. 199–206.
135 J. Dedecek, Z. Sobalik, Z. Tvaruazkova, D. Kaucky and B. Wichterlova, *J. Phys. Chem.*, 1995, **99**, 16327–16337.
136 G. Turnes Palomino, A. Zecchina, E. Giamello, P. Fisicaro, G. Berlier, C. Lamberti and S. Bordiga, in *Studies in Surface Science and Catalysis*, ed. A. Corma, F. V. Melo, S. Mendioroz and J. L. G. Fierro, Elsevier, 2000, vol. 130, pp. 2915–2920.
137 C. Lamberti, E. Groppo, G. Spoto, S. Bordiga and A. Zecchina, in *Advances in Catalysis*, ed. B. C. Gates and H. Knözinger, Academic Press, 2007, vol. 51, pp. 1–74.
138 M. Lemishka, J. Dedecek, K. Mlekodaj, Z. Sobalik, S. Sklenak and E. Tabor, *Pure Appl. Chem.*, 2019, **91**, 1721–1732.
139 J. Grzybek, B. Gil, W. J. Roth, M. Skoczek, A. Kowalczyk and L. Chmielarz, *Spectrochim. Acta, Part A*, 2018, **196**, 281–288.
140 G. Lancaster, *J. Mater. Sci.*, 1967, **2**, 489–495.
141 H. Liu, J. Wang, T. Yu, S. Fan and M. Shen, *Catal. Sci. Technol.*, 2014, **4**, 1350–1356.
142 M. Hoj, M. J. Beier, J. D. Grunwaldt and S. R. Dahl, *Appl. Catal., B*, 2009, **93**, 166–176.
143 G. Principi, *Metal*, 2020, **10**, 992.
144 H.-Y. Chen and W. M. H. Sachtler, *Catal. Today*, 1998, **42**, 73–83.
145 A. R. Overweg, M. W. J. Crajé, A. M. van der Kraan, I. W. C. E. Arends, A. Ribera and R. A. Sheldon, *J. Catal.*, 2004, **223**, 262–270.
146 Y. Li, J. Deng, W. Song, J. Liu, Z. Zhao, M. Gao, Y. Wei and L. Zhao, *J. Phys. Chem. C*, 2016, **120**, 14669–14680.
147 Y. Mao, Z. Y. Wang, H. F. Wang and P. Hu, *ACS Catal.*, 2016, **6**, 7882–7891.
148 S. Bordiga, L. Regli, D. Cocina, C. Lamberti, M. Bjørgen and K. P. Lillerud, *J. Phys. Chem. B*, 2005, **109**, 2779–2784.